



Wiley Analytical Science Virtual Conference, 2021

20 April | 4pm-5pm CEST

Correlative Raman & SEM Imaging: Current Trends and Applications

Both Raman and SEM imaging are very well-established techniques in material research and geosciences. This virtual seminar will provide an introduction to basic principles of both techniques and their use in combination. Novel and innovative application examples from different fields of research will be presented to demonstrate the advantages of the correlative approach.

Key learnings:

- How to integrate Raman and SEM into one instrument
- How to differentiate materials with the same elemental composition
- Applications from materials and earth sciences requiring correlative, nondestructive analysis techniques for their full characterization
- The basics of confocal Raman and SEM imaging

Register here

Sponsored by



Wiley Analytical Science

RESEARCH ARTICLE

Construction of saliency map and hybrid set of features for efficient segmentation and classification of skin lesion

Muhammad Attique Khan¹ | Tallha Akram² | Muhammad Sharif³ | Tanzila Saba⁴  | Kashif Javed⁵ | Ikram Ullah Lali⁶ | Urcun John Tanik⁷ | Amjad Rehman⁸

¹Department of Computer Science and Engineering, HITEC University, Museum Road, Taxila, Pakistan

²Department of Electrical Engineering, COMSATS University Islamabad, Wah Campus, Pakistan

³Department of Computer Science, COMSATS University Islamabad, Wah Campus, Pakistan

⁴College of Computer and Information Sciences, Prince Sultan University, Riyadh, SA

⁵Department of Robotics, SMME NUST, Islamabad, Pakistan

⁶Department of Computer Science, University of Gujrat, Gujrat, Pakistan

⁷Computer Science and Information Systems Texas A&M University-Commerce, USA

⁸Department of Information Systems, Al Yamamah University, Riyadh, KSA

Correspondence

Tanzila Saba, College of Computer and Information Systems, Prince Sultan University, Riyadh 11586, Saudi Arabia.

Email: drtsaba@gmail.com, attique.khan440@gmail.com

Review Editor: Paolo Bianchini

Funding information

Prince Sultan University Riyadh Saudi Arabia, Grant/Award Number: RG-CCIS-2017-06-02; Machine Learning Research Group, Grant/Award Number: RG-CCIS-2017-06-02

Abstract

Skin cancer is being a most deadly type of cancers which have grown extensively worldwide from the last decade. For an accurate detection and classification of melanoma, several measures should be considered which include, contrast stretching, irregularity measurement, selection of most optimal features, and so forth. A poor contrast of lesion affects the segmentation accuracy and also increases classification error. To overcome this problem, an efficient model for accurate border detection and classification is presented. The proposed model improves the segmentation accuracy in its preprocessing phase, utilizing contrast enhancement of lesion area compared to the background. The enhanced 2D blue channel is selected for the construction of saliency map, at the end of which threshold function produces the binary image. In addition, particle swarm optimization (PSO) based segmentation is also utilized for accurate border detection and refinement. Few selected features including shape, texture, local, and global are also extracted which are later selected based on genetic algorithm with an advantage of identifying the fittest chromosome. Finally, optimized features are later fed into the support vector machine (SVM) for classification. Comprehensive experiments have been carried out on three datasets named as PH2, ISBI2016, and ISIC (i.e., ISIC MSK-1, ISIC MSK-2, and ISIC UDA). The improved accuracy of 97.9, 99.1, 98.4, and 93.8%, respectively obtained for each dataset. The SVM outperforms on the selected dataset in terms of sensitivity, precision rate, accuracy, and FNR. Furthermore, the selection method outperforms and successfully removed the redundant features.

KEY WORDS

classification, contrast enhancement, features extraction, features selection, segmentation, skin cancer

1 | BACKGROUND

Skin cancer primarily includes two major types—malignant and benign (Papamichail et al., 2008), where malignant is largely critical and fast-

Abbreviations: H & V, Horizontal and vertical; ISIC, International skin imaging collaboration; ABCD, Asymmetry, border, color, and diameter; ANN, Artificial neural network; CAD, Computer aided design; HOG, Histogram of oriented gradient; PCA, Principle component analysis; GA, Genetic algorithm; SVM, Support vector machine; FCM, Fuzzy C-means; GVF, Gradient vector flow; LBP, Local binary pattern; FV, Feature vector; CNN, Convolutional neural network; PSO, Particle swarm optimization; EM, Expectation maximization; KNN, K-nearest neighbor; QDA, Quadratic discriminant analysis; W-KNN, Weighted-KNN; LR, Logistic regression; FPR, False positive rate; FDR, False discovery rate; FNR, False negative rate.

growing. This kind of cancer is the cause of almost 75% of total deaths among cancer patients (Jerant, Johnson, Demastes Sheridan, & Caffrey, 2000; Markovic et al., 2007). According to statistics, published by American cancer society in 2017, a total of 87,110 new cases of melanoma will be diagnosed ("Cancer Facts & Figures, 2017 is accompanied by Cancer Statistics 2017, a scientific paper published in the American Cancer Society journal, CA: A Cancer Journal for Clinicians,"). In 2018, an estimated 178,560 causes are noninvasive and 91,270 cases are invasive. An approximated 9,320 causalities are occurred including 5,880 men, and 3,330 women due to melanoma in America, in 2018 (Kimball, 2018). In Australia, the estimated number of melanoma cases in 2017 and 2018 are 13,941 and 14,320,

respectively. In 2017, 8,392 males and 8,549 females are diagnosed by skin cancer, whereas in 2018, 8,653 males and 5,667 females are diagnosed ("https://melanoma.canceraustralia.gov.au/statistics", 2018; Melanoma skin cancer in Australia, 2017). According to published statistics, significantly increasing rate are reported in last 10 to 15 years, therefore this type of cancer is receiving an utmost attention(Altekruze et al., 2010; Baldwin & Dunn, 2013; Fidler et al., 2017; Siegel, Miller, & Jemal, 2016). Melanoma is the one of the deadliest forms of skin cancer, which can be curable if detected at its earlier stages. Therefore, dermatologist tried their best to diagnose it in its early stage, to avoid its adverse effects. Dermatologists are the dermoscopic method to diagnose the skin lesion, which is a noninvasive technique. In this method, lesion structures are being analyzed with naked eyes using the magnification tool and later this information can be used to diagnose the structure by employing popular diagnostics method for example, asymmetry, border, color, and diameter (ABCD) rule (Nachbar et al., 1994), seven-Point checklist (Argenziano et al., 1998), and Menzies technique (Menzies, Ingvar, Crotty, & McCarthy, 1996). All three methods have the same first step; identification of lesion either as melanocytic (melanoma is melanocytic lesion) or nonmelanocytic, the second step differentiates melanoma and benign lesion using a score based (ABCD rule and 7-Point checklist) and features based (Menzies) approaches. In (Mayer, 1997) authors concluded that traditional dermoscopy can increase the melanoma detection rate from 10–27%. However, it depends on the formal training of dermatologist (Wolner et al., 2017). Moreover, even with these reliable diagnostic methods, it is still prone to errors and results may vary, depending on the experience of the dermatologists. One of the reliable solutions to tackle this problem is to apply computerized or digital dermoscopy analysis techniques, commonly known as computer-aided detection (CAD) system. In the field of dermatology, Stocker described the prospective benefits of digital imaging (Sáez, Acha, & Serrano, 2014). Afterwards, various efforts have been put forth through CAD systems for the improvement of clinical diagnostics of melanoma.

1.1 | Problem statement

Digital dermoscopy is a cost-effective and extensively used device to diagnose and classify skin cancer. Generally, it involves three primary steps including border extraction and segmentation, lesion representation, and classification. Automatic border detection is the most important step in the computerized analysis of dermoscopic images as it largely affects the performance of other steps. An accurate detection of lesion border is very important because accurate segmentation of lesions gives the information of irregularity and border cut-off. This process is also a challenging task due to several reasons such as different skin types, diverse lesion sizes, shapes, and colors along with various artifacts such as light and dark hair, illumination, skin lines, poor contrast, and so forth. Therefore, a robust preprocessing step plays its key role in improving the lesion's contrast, which has exceptional effects. In the later stage, the measurement of lesion features is been made for the analysis of melanoma, which requires efficient boundary detection. It is also very essential to localize the lesion in the image and calculate its measurement accurately covering asymmetry, border, irregularity of the lesion, the diameter of the extracted boundary, inaccuracy, subjectivity, poor reproducibility of human judgement, color

characteristics of the lesion area, and so forth. Feature extraction is an essential step for lesion classification and several features extraction techniques have been employed for lesion classification such as color features (C. Barata, Ruela, Francisco, Mendonça, & Marques, 2014), texture features (Haralick, Shanmugam, & Dinstein, 1973), RGB histogram features (S Chatterjee, Dey, & Munshi, 2017), deep features with convolutional auto encoder neural network (NN) (Chen, Shi, Zhang, Wu, & Guizani, 2017), and shape features (Safi et al., 2011).

1.2 | Contribution

A fusion of multiple features produces better results compared to utilization of features independently. Although, fused features have redundant information which degrades the classification accuracy. In this article, we consider above-mentioned challenges and proposed a new automated system for skin lesion detection and classification. To handle the lesion contrast problem, a new preprocessing technique is implemented on a grayscale image, which enhances the contrast by reducing light variations of the lesion area. Secondly, a novel saliency-based segmentation algorithm is also implemented on the grayscale image. The proposed technique efficiently segments the lesion area compared to existing segmentation methods. For testing, we utilized publicly available dataset PH2 and provided maximum segmentation accuracy of 96.71%. The sample images from the PH2 dataset are shown in Figure 1. Finally, a set of four selected features are utilized for the accurate classification of melanoma and nonmelanoma. Selected features include, horizontal & vertical, global, shape, and texture. To overcome the problem of the *curse of dimensionality*, principle component analysis (PCA) based dimensionality reduction technique is utilized, which reduces the HOG features which are later appended with other set of features using the serial based method. In the later stage, fused features are optimized using the serial based method. In the later stage, fused features are optimized using a genetic algorithm (GA) to select optimal features based on a selected threshold values. The optimized features are finally classified using support vector machine (SVM). Our major contributions are listed below.

1. A contrast stretching technique is implemented for improving the lesion contrast. Initially, the blue channel is selected from RGB image based on their best pixels information and performed a top-hat filter. Afterwards, calculate the cumulative mean of a top-hat filtered image and perform a logarithmic operation for removing the illumination effects.
2. For extraction of lesion region, extract color, and shape features of an image and combine in one vector. The cumulative mean is calculated from a fused vector and subtract it from the contrast stretching the image. The LAB color space is performed on the original image and extracts the luminance channel, which is later added into difference image for construction of the saliency map. Finally, a threshold function is implemented on saliency mapped image for lesion extraction.
3. Extract four types of features such as shape, texture, horizontal and vertical, and geometric of extracted region. The PCA is implemented on shape features because of high dimensionality. Therefore, select

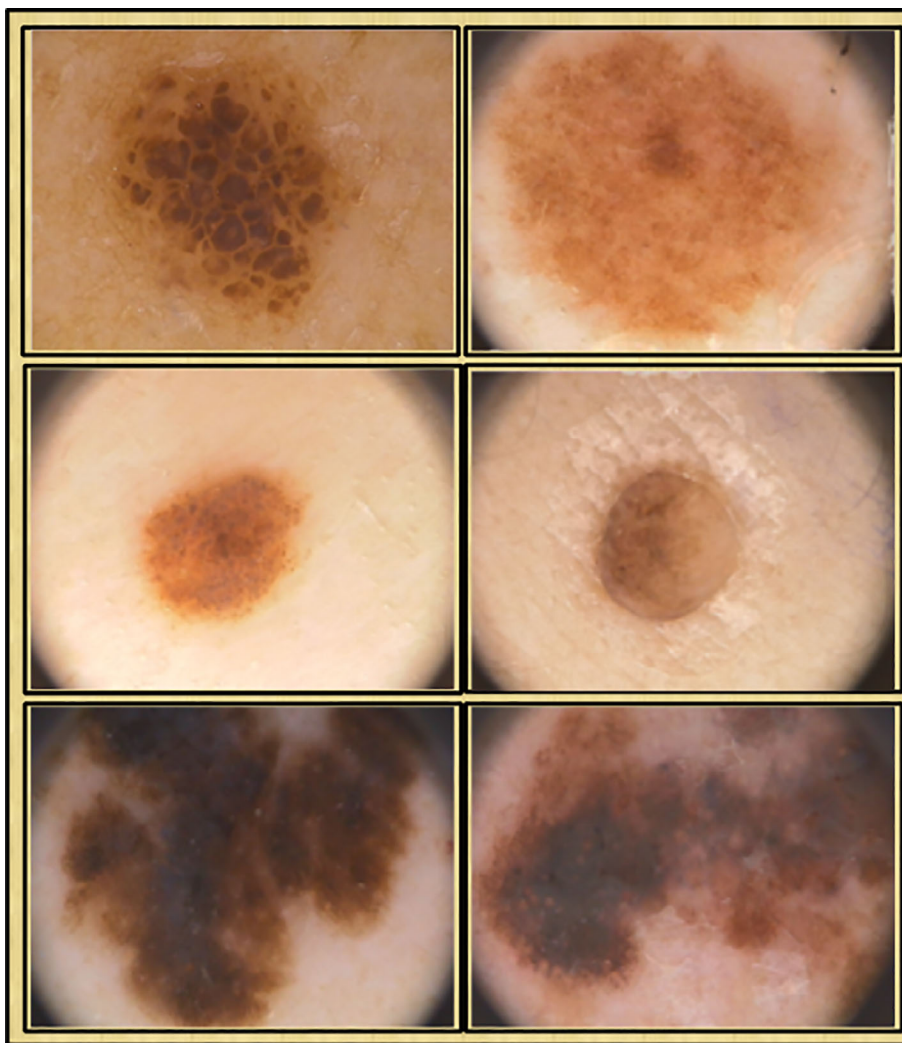


FIGURE 1 Sample lesion images: First row atypical nevus; second row common nevus; third row melanoma [Color figure can be viewed at wileyonlinelibrary.com]

2,368 features from 236,880, which are later fused with other extracted features prior to feature selection step using GA.

(A. C. F. Barata, 2017; Fahad, Ghani Khan, Saba, Rehman, & Iqbal, 2018; Iqbal, Khan, Saba, & Rehman, 2017, Iqbal, Ghani, Saba, & Rehman, 2018; Mughal, Muhammad, Sharif, Rehman, & Saba, 2018). Similarly, several machine learning techniques are also adopted in literature for lesion detection and classification such as adaptive thresholding, k-means clustering (Agarwal, Issac, Dutta, Riha, & Uher, 2017), fuzzy c-means (FCM) clustering (Masood & Al-Jumaily, 2013), inutile fragment removal methods (Majtner, Lidayova, Yildirim-Yayilgan, & Hardeberg, 2016), region growing methods (Mohamed et al., 2017), gradient vector flow (GVF) snakes (Flores & Scharcanski, 2016), Markov random field, convolution autoencoder NN (Chen, Shi, et al., 2017), and region fusion based multimodal technique (Yuan, Situ, & Zouridakis, 2009). Saptarshi Chatterjee, Dey, and Munshi (2018) introduced a wavelet packet decomposition patterns for texture feature extraction to differentiate the melanoma and benign. Then, a feature selection algorithm is proposed, which is worked with SVM to reduce the irrelevant features. The radial basis function is used for SVM and achieved the best classification accuracy 98.28%.

Haidi et al. (Fan, Xie, Li, Jiang, & Liu, 2017) introduced a new saliency method in combination with the Otsu segmentation method for accurate lesion extraction. The method primarily incorporates

2 | RELATED WORK

Lately, several methods have been introduced for automatic detection and classification of skin lesion, which may help doctors for efficient diagnosis. However, for an accurate lesion classification of several patients, hundreds of images need to be processed manually, therefore there is a requirement for an intelligent healthcare system (Chen et al., 2017; Chen, Ma, Song, Lai, & Hu, 2016; Rehman et al., 2018,b,c; Sadad, Munir, Saba, & Hussain, 2018; Zhang, Qiu, Tsai, Hassan, & Alamri, 2017). The existing computer vision based methods have shown improved accuracy for border detection and finally lesion calculation. In most of the existing literature, certain preprocessing steps (color correction/brightness, contrast enhancement) played a significant role in an accurate border detection, which leads to accurate classification (Nasir et al., 2018). Lately, several research studies are giving a special attention on color correction obtained or color space transformations

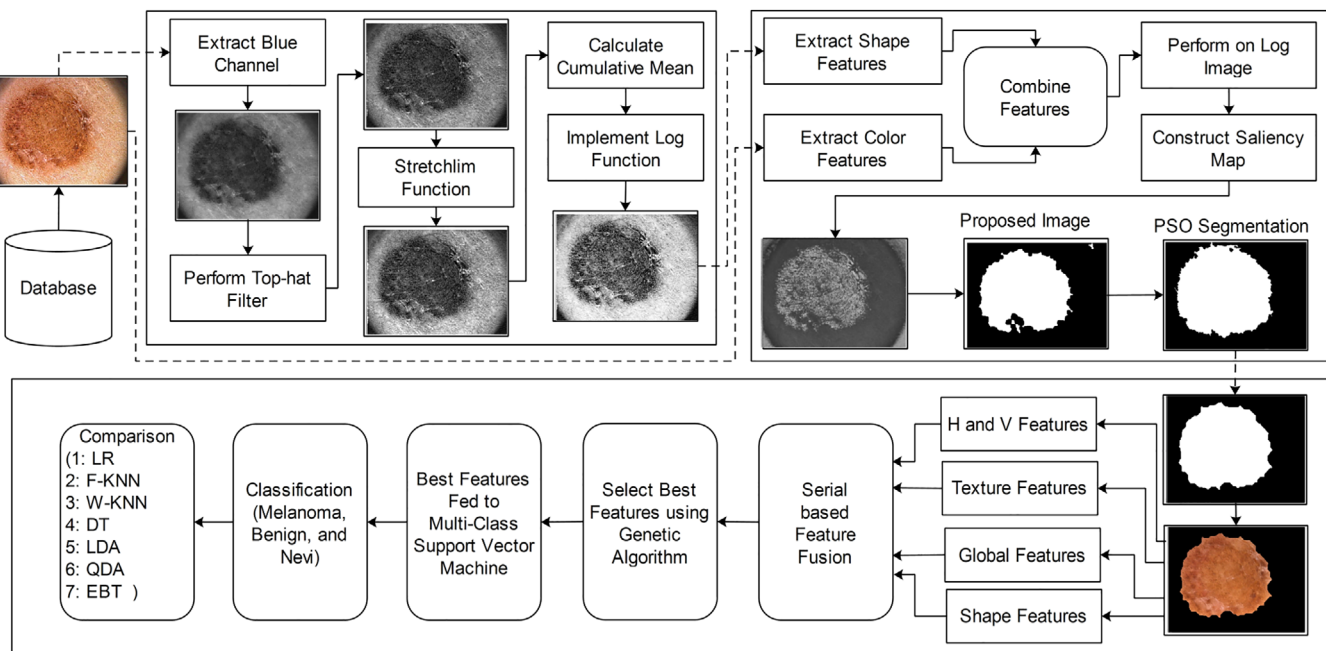


FIGURE 2 Proposed flow diagram for skin lesion detection and classification [Color figure can be viewed at wileyonlinelibrary.com]

two major steps including, preprocessing and segmentation of lesion. In the preprocessing step, lesion regions are enhanced using healthy skin information and later construct a color and brightness saliency map. The introduced method is validated on three datasets as well as PH2, EDRA, and ISBI, and showed improved performance. Similarly, Bill et al. (Lin, Michael, Kalra, & Tizhoosh, 2017) compared the U-Net segmentation method with C-Means clustering. In the first step, they implemented U-net segmentation technique after a preprocessing step of histogram equalization. In the second step, they applied the C-Means clustering method to segment the skin lesion. The experimental results revealed that the U-Net method successfully achieved better performance in terms of improved Jaccard index compared to clustering. Also, the implementation of

histogram equalization as a preprocessing step improved the U-Net segmentation accuracy. Satheesha, Satyanarayana, Prasad, and Dhruve (2017) presented a noninvasive 3D reconstruction method for skin lesion classification. The 3D shape and depth features are extracted from the 3D reconstruction method in addition to color, shape, and texture features. For evaluation of the presented method, PH2 and ATLAS dataset are used and achieved 96 and 98% sensitivity rate. Rui et al. (Fonseca-Pinto & Machado, 2017) introduced a new automated approach for skin lesion classification from dermoscopic images using texture scale based features. Initially, authors decomposed the input dermoscopic image into a bi-dimensional empirical model. Later, extracted local binary pattern (LBP) variance features and plugged into the Ada-Boost algorithm

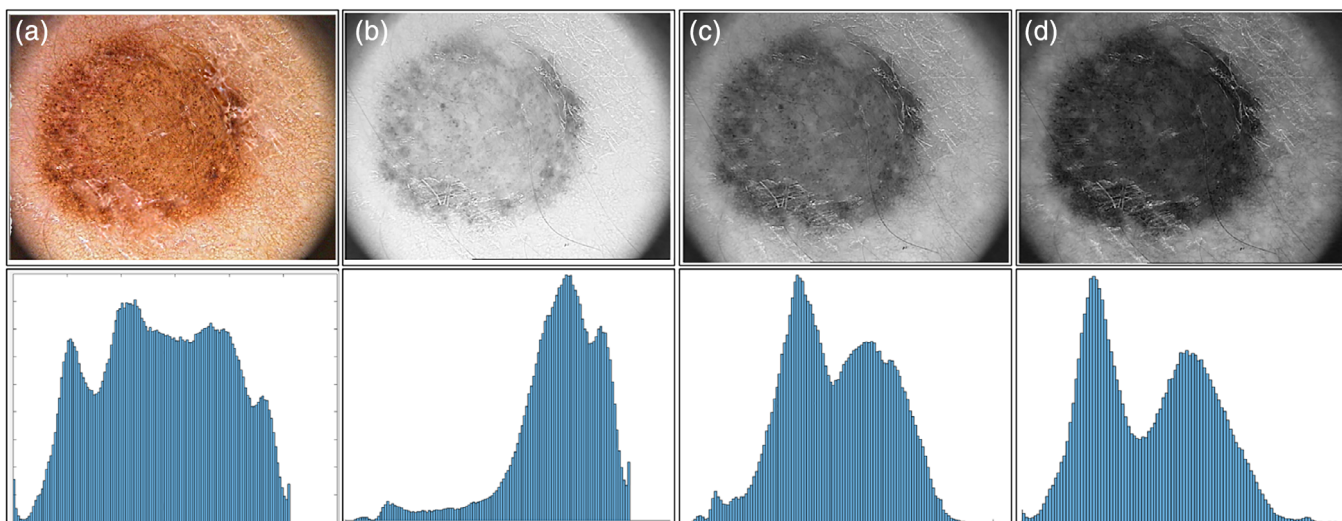


FIGURE 3 Selection of blue channel based of their highest intensity values. (a) Original image; (b) Red channel; (c) Green channel; (d) Blue channel [Color figure can be viewed at wileyonlinelibrary.com]

for classification. Huiyu et al. (Zhou, Schaefer, Sadka, & Celebi, 2009) proposed a novel mean-shift based fuzzy C-means algorithm with an advantage of less computational time compared to existing techniques. Zhen et al. (Z. Yu et al., 2017) presented a hybrid convolutional neural network (CNN), SVM, and Fisher Vector based method for lesion classification from dermoscopic images. Initially, the pretrained models are used for feature extraction from original images. Later the encoded features are classified using SVM. The evaluations result of the presented method are compared with traditional low-level features and showed improved performance. Mahbod, Ecker, and Ellinger (2017) introduced a new fully automated method for skin lesion classification using pretrained CNN features. The extracted features are classified by ensemble learning and showed improved performance on international skin imaging collaboration (ISIC) 2017 dataset.

The aforementioned studies discuss the importance of lesion enhancement, which is the one, the primary steps for an accurate classification. For image segmentation, they mostly utilize well-known techniques such as K-means, watershed, Fuzzy C-means, Otsu thresholding and to name a few (Abbas et al., 2016, 2018; Husham, Alkawaz, Saba, Rehman, & Alghamdi, 2016; Jamal, Hazim Alkawaz, Rehman, & Saba, 2017; Norouzi et al., 2014; Saba et al., 2018,b; Waheed, Alkawaz, Rehman, Almazyad, & Saba, 2016). The saliency methods are also employed for lesion segmentation with improved performance. Later, in the classification phase, color, and texture features are mostly employed, which are later classified using SVM or other classifiers. In this study, we implement a saliency method-based contrast stretching and later shape and texture features are extracted, which after passing through feature selection step are finally classified using SVM.

3 | METHOD AND MATERIALS

A new technology has been constructed for lesion segmentation and recognition in terms of melanoma and nonmelanoma. The proposed approach consists of lesion preprocessing, lesion segmentation and border extraction, features extraction and selection, and classification. The brief descriptions of major steps are given below:

(a) In the preprocessing step, the blue channel is selected and contrast is enhanced by calculating the mean of the top-bottom filtering image and log transformation is performed to enhance the contrast of lesion area in comparison to the background; (b) A saliency map is constructed by finding the cumulative mean of enhanced image and completing the results in luminance channel by making use of LAB transformation. Finally, the threshold function is set for the constructed lesion region; (c) feature vector of size $1 \times 2,546$ is formed, which is used by new features selection technique as a Genetic algorithm on the combination of features as shape, texture, global and horizontal, and vertical. Finally, the selected features are classified by the SVM. The detailed block diagram of the proposed skin lesion detection and classification methodology is shown in Figure 2. Description of each step is illustrated in the succeeding sections.

3.1 | Preprocessing

The preprocessing step is important for resolving the problem of poor contrast. Before resolving the contrast problem, first hairs from lesion area are removed because hairs on the lesion area affect the segmentation of lesion. In literature, many methods have been implemented for hair removals (Kasmi & Mokrani, 2016; Lee, Ng, Gallagher, Coldman, & McLean, 1997; Mirzaalian, Lee, & Hamarneh, 2014; Mughal et al., 2017a,b,c). In this research work, the improved DullRazor technique (Kiani & Sharafat, 2011) is utilized, which work better as compared to Lee et al. (1997). The improved technique is a combination of Prewitt filter and orientation of hairs. Then the contrast of lesion area is enhanced by implementing a new technique which consists of two major steps: (a) top-bottom filtering; (b) contrast stretching and log transformation. The detail of each step is defined below.

3.1.1 | Top-bottom hat filtering

The top-bottom hat filtering technique enhancing the contrast of lesion area with respect to maximum and minimum intensity values. The top-bottom filter is performed on blue channel $\psi^B(x, y)$, which is extracted from original image $\psi(x, y)$ as shown in Figure 3. From Figure 3, the selection of $\psi^B(x, y)$ channel provides better intensity values as compared to red and green channels.

The blue channel $\psi^B(x, y)$ defined as:

$$\psi^B(x, y) = \frac{\psi^B}{\sum_{j=1}^3 \psi^j} \quad (1)$$

Where $j = 1, 2, 3$ an index for red, green, and blue channels. Then perform top-bottom hat filtering technique for enhancing the contrast of lesion. The top-hat filter is work for foreground objects and bottom-hat for background objects. The top-bottom hat filters are defined as:

$$\psi_{top}(x, y) = \psi^B(x, y) - \psi^B(x, y) \circ S \quad (2)$$

$$\psi_{bot}(x, y) = \psi^B(x, y) \bullet S - \psi^B(x, y) \quad (3)$$

Where $\psi_{top}(x, y)$ define as top-hat filtering image, $\psi^B(x, y)$ is selected blue channel, $\psi_{bot}(x, y)$ is bottom-hat image \circ denotes the opening operation, \bullet represents closing operation, and S represents the structuring element. The structuring element place at the possible location of the input image and compared with corresponding neighbourhood pixels. The basic purpose of structuring element is to check those regions which are fits with neighbourhood pixels. For top-bottom filtering, S initialized as nine, which means the window size is 9×9 across the input image. Then relate both images $\psi_{top}(x, y) = \psi^B$ and $\psi_{bot}(x, y)$ as:

$$\psi_R(x, y) = \psi_{top}(x, y) + \psi^B(x, y) \quad (4)$$

$$\psi_{Ft}(x, y) = \psi_R(x, y) + \psi_B(x, y) \quad (5)$$

Where $\psi_R(x, y)$ define relation between top-hat image and original image and $\psi_{Ft}(x, y)$ define final top-bottom filtering image. To adjust the image intensities and find out the limits of contrast image, perform stretchlim MATLAB function. The stretchlim function return the

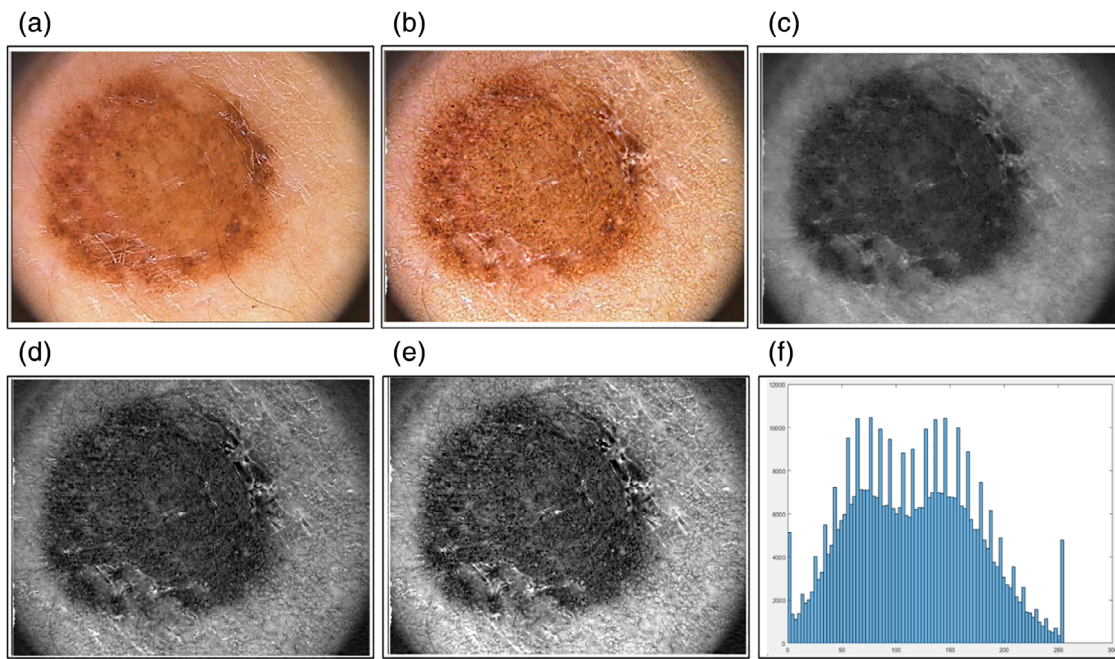


FIGURE 4 Top-bottom hat filtering results. (a) Original image; (b) Hair removal image; (c) Selected blue channel; (d) Top-bottom hat filtering; (e) Adjust intensities and stretchlim image; (f) Histogram of stretchlim image [Color figure can be viewed at wileyonlinelibrary.com]

minimum and maximum intensity value of an image, which is defined as follows:

$$\begin{aligned}\psi_{\min} &= \text{Min}(\psi_{Ft}(x, y)) \\ \psi_{\max} &= \text{Max}(\psi_{Ft}(x, y)) \\ \text{Diff} &= \psi_{\max} - \psi_{\min} \\ \psi_{\text{scale}} &= \frac{\text{pix}_i - \psi_{\min}}{\text{Diff}} \\ \psi_F(x, y) &= \psi_{\text{scale}}(\psi_{Ft}(x, y))\end{aligned}\quad (6)$$

Where ψ_{\min} denotes the minimum pixel value of an image $\psi_{Ft}(x, y)$, ψ_{\max} is maximum pixel value, Diff is difference between maximum and minimum pixels, and ψ_{scale} denotes the linear scaling function. Finally, round the values of scaling function and obtain an enhanced image $\psi_F(x, y)$ as shown in Figure 4e.

3.2 | Contrast stretching and log transformation

The contrast stretching operation is performed on $\psi_F(x, y)$. For contrast stretching, first the cumulative mean of $\psi_F(x, y)$ image is calculated to obtain the average intensity value. The cumulative mean is a sequence of partial mean of number of pixels in the image.

$$\mu_c = x_1 + x_2 + \dots + x_N \quad (7)$$

Where x_1, x_2, \dots, x_i are number of pixels, μ_c denotes the cumulative mean, and N represents the total number of pixels in the image $\psi_F(x, y)$. Then the partial mean is defined as:

$$\mu_c = \sum_{i=1}^N x_i \quad (8)$$

Where $i \in 1$ to N . Then, a contrast stretching method is used on $\psi_F(x, y)$ to enhance the contrast lesion in order to make the infected region more visible. The contrast stretching function is defined as:

$$\psi_{cnt}(x, y) = \frac{\mu_c}{\psi_F(x, y) + \epsilon} \quad (9)$$

Where $\psi_{cnt}(x, y)$ represents contrast stretching image, μ_c defines the cumulative mean of $\psi_F(x, y)$, ϵ defines a scaling parameter which is initialized to two. Finally, a logarithmic function is implemented to remove the effect of illumination and to make the lesion region more visible as compared to $\psi(x, y)$, $\psi_F(x, y)$, and $\psi_{cnt}(x, y)$. The logarithmic function is implemented as:

$$\psi_{\log}(x, y) = \gamma \times Z_1 \quad (10)$$

Where $\psi_{\log}(x, y)$ is a logarithmic image, γ is a constant parameter which is initialized to one, and $Z_1 = \text{Log}(1 + \psi_{cnt}(x, y))$. The results of contrast stretching are shown in Figure 5.

3.3 | Border detection

In the computerized analysis of dermoscopic images, the accurate interpretation of border detection is a primary step. The accurate border detection against lesion area is important to measure the segmentation performance in terms of clinical features such as irregularity and asymmetry of the border area. In this work, a saliency map has been constructed for accurate border detection using the combination of color and shape based features. The saliency map provides higher responses to more important regions in the input image. The purpose of construction saliency map is to easily visualize the lesion area or to make a representation of image more meaningful.

To construct a saliency map, initially, the HOG features are extracted from enhanced logarithmic image and color features are extracted from original image as shown in Figure 2. Then, these features are combined and performed on the logarithmic image, $\psi_{\log}(x, y)$. After that, the cumulative mean of $\psi_{\log}(x, y)$ is calculated

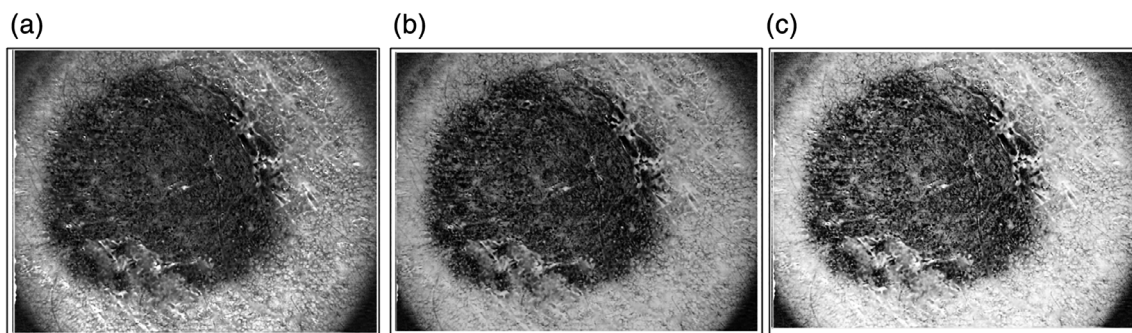


FIGURE 5 Contrast stretching results. (a) Stretchlim image; (b) Contrast stretching image; (c) Logarithmic image

as $\mu = \frac{\sum x_i}{N}$, where x_i denotes the number of pixels in $\psi_{\log}(x, y)$ and N denotes total number of pixels as discussed above in Section 3.2. Then determine the difference as follows:

$$\psi_{dif}(x, y) = \mu - \psi_{\log}(x, y) \quad (11)$$

Here $\psi_{\log}(x, y)$ represents the pixel value of the logarithmic enhanced image. After this, the luminance transformation is calculated from LAB color space in order to add their pixel values in $\psi_{dif}(x, y)$ for making the initial map of lesion area. The LAB transformation is computed from the original image and select the Luminance channel for further operation. The luminance channel gives more information as shown in the Figure 6 because their histogram values clearly indicate the lesion area. The luminance transformation is computed as:

$$\psi_L(x, y) = \delta \times f(\psi_x) - 16 \quad (12)$$

Where δ is an integer value which initialized to 116, $\psi_x \in \lambda$, $\lambda = W \times \psi_v$, $\psi_v = \psi_B$, and $W = 93.04$ and f denotes the function (Hsiao, Yen, & Lee, 2017), which is defined as follows:

$$f(x) = \begin{cases} (x)^{\frac{3}{2}} & \text{if } x > \delta^3 \\ \frac{x}{3\delta^2} + \frac{4}{29} & \text{Otherwise} \end{cases} \quad (13)$$

The assigned value of δ is selected for all type of dermoscopic images because it gives more information as other integer values. Hence,

$$\psi_{map}(x, y) = \psi_L(x, y) + \psi_{dif}(x, y) \quad (14)$$

$$= \sum(\psi_L(x, y), \psi_{dif}(x, y)) \quad (15)$$

The size of both images is 512×512 . Then, Median filter and Wiener filter of size 3×3 and 5×5 are applied respectively. The Median filter utilized for removing the noise from images and Wiener filter works on blur region in the images. These filters are utilized for improving the segmentation accuracy. The final saliency map is defined as:

$$F_{thr}(x, y) = \begin{cases} 1 & \text{if } \psi_{map}(x, y) \geq 0.524 \\ 0 & \text{if } \psi_{map}(x, y) < 0.524 \end{cases} \quad (16)$$

Thus, threshold function $F_{thr}(x, y)$ is performed on $\psi_{Fmap}(x, y)$, which is a final mapped image. The threshold function is applied as:

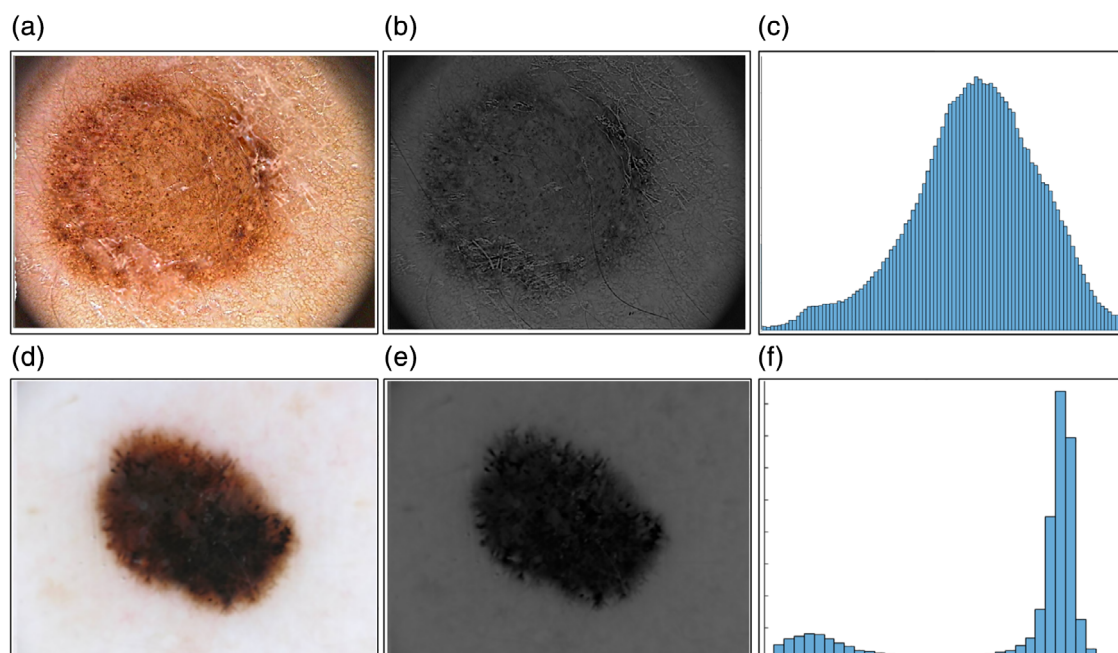


FIGURE 6 Selection of luminance channel. (a) Original image for PH2 dataset; (b) Luminance channel; (c) Histogram values; (d) Original image for ISIC dataset; (e) Luminance channel; (f) Histogram representation [Color figure can be viewed at wileyonlinelibrary.com]

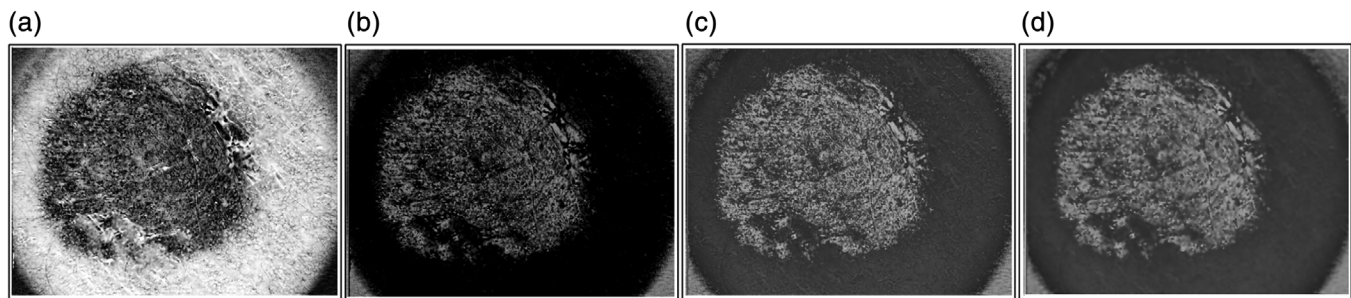


FIGURE 7 Saliency mapped results. (a) Logarithmic image; (b) Difference of mapped image; (c) Initial mapped image; (d) Final mapped image after performing morphological operations

$$\psi_{pro}(x, y) = F_{thr}(x, y)(\psi_{Fmap}) \quad (17)$$

In order to make the segmentation results more efficient (obtained maximum accuracy for segmentation), an existing particle swarm optimization (PSO) based segmentation technique (Chander, Chatterjee, & Siarry, 2011) has been implemented. The term efficient described that achieved maximum segmentation accuracy and reduce the error rate. Therefore, the PSO method is utilized to optimize the segmentation accuracy while working with the proposed segmentation method. The optimization of PSO segmentation is to get the maximum and minimum values of the dermoscopic image and also iterate each pixel up to N times. Through PSO segmentation the whole lesion region is extracted and fused with purpose saliency method for optimization of efficient lesion extraction. Some other methods such as Otsu thresholding, expectation maximization (EM) segmentation (Glaister, Wong, & Clausi, 2014) and Fuzzy C mean clustering (Masood & Al-Jumaily, 2013) methods do not perform well for all dermoscopic image because of the irregularity of the lesion, change in a border

location, and change in brightness. The fitness function for PSO segmentation is defined as:

$$\psi_{PSO}(x, y) = \eta \times (\max(\psi_{Fmap})) + \min(\psi_{Fmap}) \quad (18)$$

Where maximum intensity value is set to 256, population size is 100, a number of iterations are 500, individual weight for each intensity value is 0.5, social weight is selected as 0.5, and the inertial factor is initialized to one. The η is the constant parameter having randomly selected value between 0 and 1. The above fitness function calculates the maximum and minimum pixels values from saliency mapped image and then performing some addition and subtraction operation for optimization of lesion segmentation. The PSO optimization performs well as compare to other segmentation algorithms as shown in the Figure 8, which is clear that the implemented PSO segmentation algorithm works well for challenges such as irregularity and border change. Then a weighted function is obtained on $\psi_{PSO}(x, y)$ and $\psi_{pro}(x, y)$ segmented images which are fused with each other. The weighted

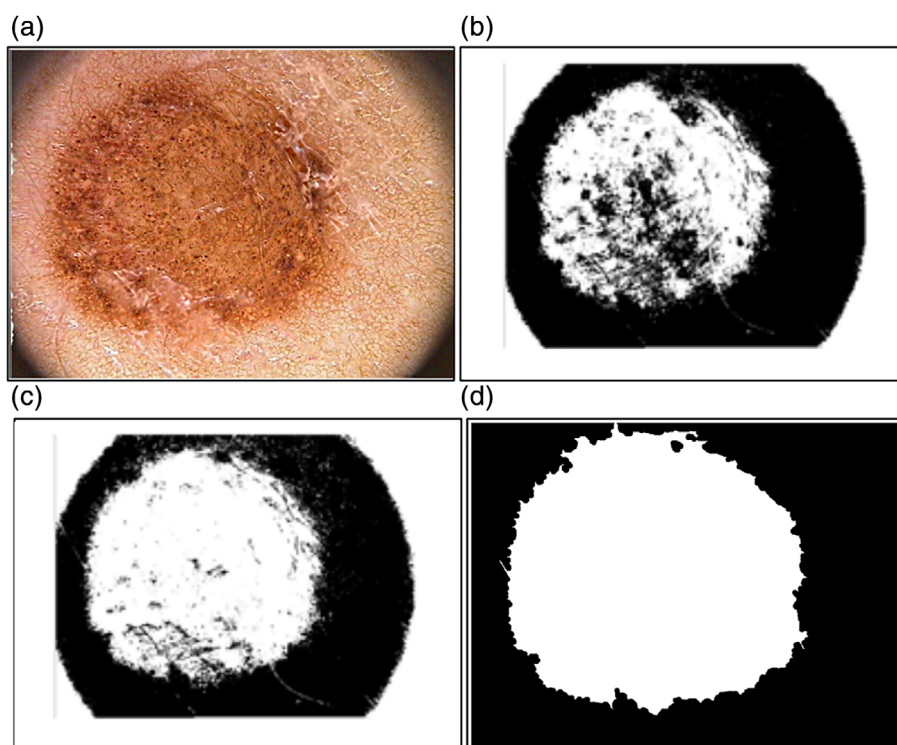


FIGURE 8 Different segmentation method results. (a) Original image; (b) Otsu thresholding image; (c) EM segmentation image; (d) PSO segmentation [Color figure can be viewed at wileyonlinelibrary.com]

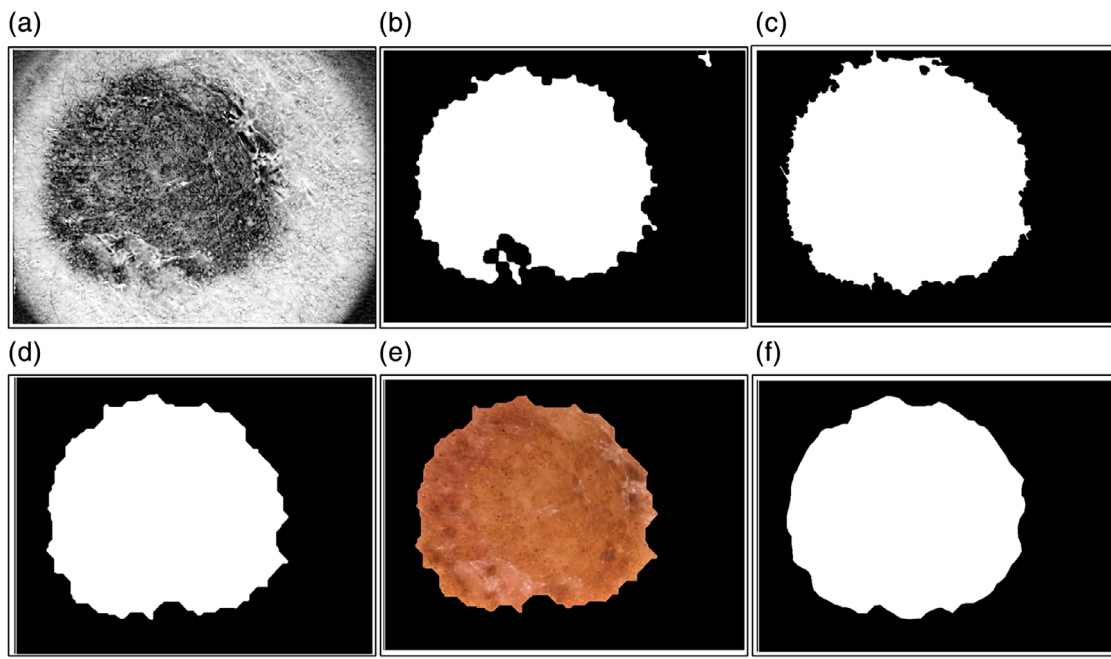


FIGURE 9 Final segmentation results. (a) Logarithmic image; (b) Proposed segmentation results; (c) PSO optimization results; (d) Final segmentation after performing weight function and morphological operation; (e) Mapped final segmented image on original image; (f) Ground-truth image [Color figure can be viewed at [wileyonlinelibrary.com](#)]

function determines the pixels values such as their sum is ≥ 1 and < 1 . The pixels which are ≥ 1 are represented the lesion and else are background. The weighted function is defined as:

$$W(x) = \begin{cases} 1 & \text{if } \sum(\psi_{pso}(x, y), \psi_{pro}(x, y)) \geq 1 \\ 0 & \text{if } \sum(\psi_{pso}(x, y), \psi_{pro}(x, y)) < 1 \end{cases} \quad (19)$$

The optimized saliency image can now be determined as:

$$\psi_{opt}(x, y) = W(\psi_{pro}(x, y), \psi_{pso}(x, y)) \quad (20)$$

The weighted function fused both images according to Equation 21. The detailed description of PSO optimization for lesion segmentation is described in Algorithm. Finally, some morphological operations (such as closing, filling, dilation, and area removal) are carried out for further enhancing the accuracy of segmentation. The utilized morphological operations are defined as follows:

$$\psi_{opt}(x, y) \bullet S_1(x, y) = (\psi_{opt} \oplus S_1) \ominus S_1 \quad (21)$$

$$\psi_{opt}(x, y) \ominus S_1(x, y) = \min_{u, v} (\psi_{opt}(x - u, y - v) + S_1) \quad (22)$$

$$FL(f) = R_f^c(\psi_{opt}) \quad (23)$$

$$\psi_{opt}(x) = \begin{cases} f(x), & \text{if } x \text{ lies on border} \\ t_{\max}, & \text{Otherwise} \end{cases} \quad (24)$$

From Equations 23, 24, and 25 • denotes the closing operation, \ominus is dilation operation, and $FL(f)$ is filling operation. The structuring element (S_1) initialized to seven. Hence, the final segmented image is determined as:

$$\psi_{F\ sal}(x, y) = \varphi(\psi_{opt}(x, y)), \varphi \in [\bullet, \ominus, FL(f)] \quad (25)$$

Algorithm PSO based saliency optimization algorithm.

```

1: Output:  $\psi_{F\ sal}(x, y) \leftarrow$  Optamized Saliency Image.
2: Input:  $\psi_{pro}(x, y) \leftarrow$  Proposed Saliency Image
3: Max Intensity  $\leftarrow 256$ ;
4: Population Size  $\leftarrow 100$ ;
5: Iterations  $\leftarrow 500$ ;
6: Individual Weight  $\leftarrow 0.5$ ;
7: Social Weight  $\leftarrow 0.5$ ;
8: InertialFactor  $\leftarrow 1$ ;
9:  $N_{TH} \leftarrow 1$ ;
10: C  $\leftarrow [01]$ ;
11: FOR (i : 1 to 500)
12: FOR (j : 1 to  $N_{TH}$ )
13:  $\text{Max}(P_x) \leftarrow 256 \times \sum_{k=1}^2 W_k$ 
14:  $\text{Min}(P_x) \leftarrow \sum_{k=1}^2 W_k$ 
15: End FOR
16: Perform Equation 20  $\leftarrow \psi_{pso}(x, y)$ 
17: Implement Weighted Function  $\leftarrow W(x)$ by Equation 21;
18: End FOR

```

The segmentation results are shown in Figure 9. From Figure 9, (a) denotes the enhanced logarithmic image, which is obtained from Equation 11, (b) denotes the proposed segmented image, which is obtained from Equations 12–19, (c) denotes the PSO segmented image, and (d) is final optimized image, which is generated from Equation 27.

3.4 | Analysis

To determine the accuracy of the proposed segmentation algorithm, the analysis is done with ground truth values in terms of

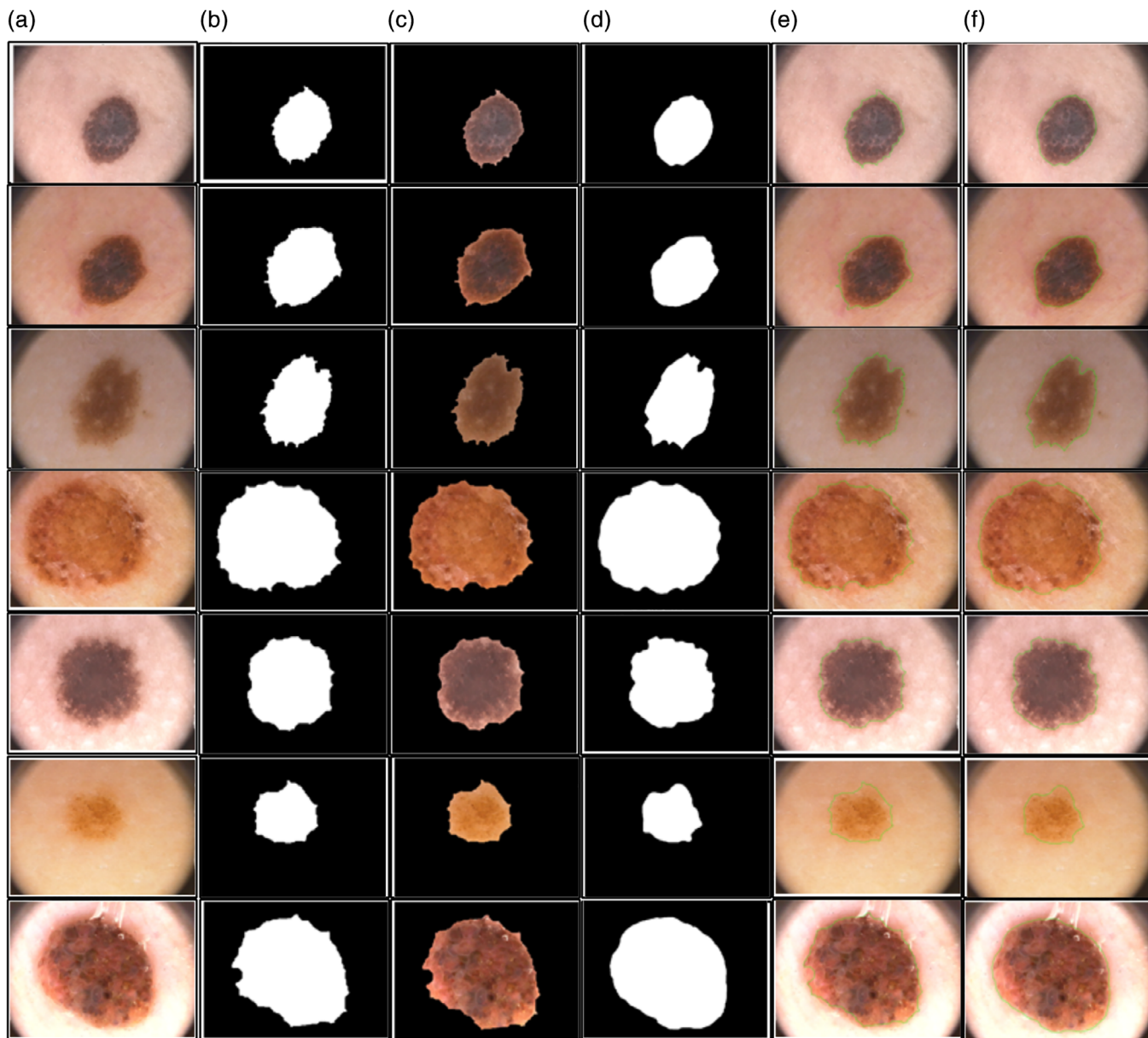


FIGURE 10 Analysis of proposed segmentation results with ground truth image: (a) Original image; (b) Segmented image; (c) Mapped segmented image on original image; (d) Ground truth image; (e) Border draw on original image by segmented image; (f) Border based on ground truth image [Color figure can be viewed at wileyonlinelibrary.com]

graphical and tabular form. Eighteen lesion images have been randomly selected from PH2 dataset having their respective ground truth images. The selected images consist of three different types that is, melanoma, common nevi, and atypical nevi. The visual results are also shown in Figure 10 with their respective ground truth and border. Moreover, tabular analysis, including Accuracy, Dice, Jaccard index, Jaccard distance, segmented diameter, and ground truth diameter are calculated. The millimeter unit is used to measure the value of ground truth and segmented diameter. These measures are determined as:

$$\text{Diameter} = \sqrt{\frac{4 \times \text{Area}}{\pi}} \quad (26)$$

$$\text{JaccardIndex} = \frac{N_m}{D_m} \quad (27)$$

$$\text{JaccardDistance} = 1 - \text{JaccardIndex} \quad (28)$$

$$\text{Dice} = \frac{2 \times \text{NZ}(\psi_{opt}(x, y), \psi_{gtr}(x, y))}{\text{NZ}(\psi_{opt}(x, y), \psi_{gtr}(x, y))} \quad (29)$$

Where $N_m = \psi_{opt}(x, y) \cap \psi_{gtr}(x, y)$, $D_m = \psi_{opt}(x, y) \cup \psi_{gtr}(x, y)$ and $\psi_{gtr}(x, y)$ is ground truth image. The Area represents the total number of ON pixels in the proposed segmented image. The ON pixel denotes by 1 and Off pixel denotes by 0.

$$\text{Accuracy} = \frac{C_i}{\text{seg}(x, y) + \text{gtr}(x, y) - C_i} \times 100 \quad (30)$$

Here $\text{seg}(x, y)$ and $\text{gtr}(x, y)$ represent the final segmented image and ground truth image and C_i denotes the common pixels of the segmented image and ground truth image. From Table 1, it is clear that

TABLE 1 Proposed segmented lesion accuracy for PH2 dataset

Comparison of segmented lesion with groundtruth for PH2 dataset							
Sr#	Image id	Dice	Final score	Jaccard index	Jaccard distance	Segmented diameter mm	Groundtruth diameter mm
1	IM003	0.9425	2	0.9413	0.0587	247.29	252.00
2	IM004	0.9553	2	0.9645	0.0355	335.62	329.71
3	IM016	0.9623	3	0.9227	0.0773	315.55	306.51
4	IM017	0.9658	3	0.9463	0.0537	509.72	520.90
5	IM020	0.9639	1	0.9604	0.0396	259.64	257.73
6	IM021	0.9360	2	0.9222	0.0778	281.17	274.08
7	IM025	0.9675	2	0.9671	0.0329	310.59	313.17
8	IM036	0.9715	2	0.9646	0.0354	478.75	483.90
9	IM041	0.9672	2	0.9564	0.0436	367.53	365.58
10	IM075	0.9556	2	0.9450	0.0550	356.71	361.28
11	IM078	0.9722	2	0.9388	0.0612	342.58	335.70
12	IM105	0.9513	2	0.9124	0.0876	241.51	233.42
13	IM150	0.9689	3	0.9328	0.0672	459.21	470.89
14	IM169	0.9760	2	0.9630	0.0370	352.45	352.01
15	IM171	0.9690	2	0.9398	0.0602	280.12	280.52
16	IM173	0.9560	2	0.9357	0.0643	376.78	387.61
17	IM198	0.9538	2	0.9417	0.0583	263.07	261.10
18	IM427	0.9516	2	0.9376	0.0624	416.66	428.66

the maximum accuracy is 96.71% with segmented diameter 310.59 and ground truth diameter is 313.17. In addition, the segmentation performance is computed on ISBI 2016 dataset in the form of accuracy and FNR. The few best results are given in Table 1-A. The maximum achieved segmentation accuracy 98.88% and average accuracy is 95.989% which is superior as compare to recent state-of-the-art techniques (Rahman, Alpaslan, & Bhattacharya, 2016; Sarker et al., 2018; Yu, Chen, Dou, Qin, & Heng, 2017).

4 | FEATURES EXTRACTION AND SELECTION

In the field of pattern recognition, the feature extraction is a key term for representation of an image. Four types of features are extracted to solve the problem of efficient classifications. In this section, we consider that the problem of appropriate features extraction and selection. The name of an extracted set of features is horizontal and vertical splitting feature (H & V), global features, shape-based features, and gray level co-occurrences matrix (GLCM) features. The GLCM features represent the texture representation of an object. The brief description of each feature descriptors is given below.

4.1 | H & V splitting features

In H & V features extraction phase, the four cropping parameters are utilized which are top-row splitting, bottom-row splitting, left-column splitting, and right-column splitting. For horizontal and vertical splitting, true pixels are initialized zero at x-axis and y-axis. Rows pixels and columns pixels are also initialized to zero. Then, an updated function is implemented to update the row and column pixels values on every iteration. On each iteration, the updated values replace the previous row and column pixel values and this process is continued until

the number of iterations is not executed. The updated function is defined as:

$$f(\varphi_{update}) = \begin{cases} \text{update } (R_x) \text{ for } R_p(x) + H_r \\ \text{update } (C_y) \text{ for } C_p(y) + V_c \end{cases} \quad (31)$$

Where update (R_x) denotes the updated row, update (C_y) is updated column, $R_p(x)$ represents total number of row pixels, $C_p(y)$ represents total number of column pixels, $H_r \in j \times R_x$ and $V_c \in k \times C_y$. Hence, the final horizontal and vertical vectors are computed as:

$$\gamma_x = \frac{R_p(x)}{\varphi_{total}(x, y)} \quad (32)$$

$$\gamma_y = \frac{C_p(y)}{\varphi_{total}(x, y)} \quad (33)$$

TABLE 1-A 1: Segmentation accuracy results on ISBI 2016 dataset

Image #	Accuracy (%)	FNR (%)	Image #	Accuracy (%)	FNR (%)
1	98.88	1.12	14	97.98	2.02
2	98.79	1.21	15	97.91	2.09
3	98.71	1.29	16	97.82	2.18
4	98.61	1.39	17	97.79	2.21
5	98.59	1.41	18	97.71	2.29
6	98.59	1.41	19	97.67	2.33
7	98.57	1.43	20	97.56	2.44
8	98.40	1.60	21	97.42	2.58
9	98.19	1.81	22	97.33	2.67
10	98.10	1.90	23	97.31	2.69
11	98.07	1.93	24	97.22	2.78
12	98.01	1.99	25	97.16	2.84
13	98.01	2.99	26	97.07	2.93
Overall average				95.989	

Where γ_x represents the horizontal feature vector, γ represents the vertical feature vector, $\varphi_{total}(x, y) = \sum (R_p(x), C_p(y))$ represents the total number of pixels in the segmented image. From this process, a feature vector of size 1×60 is constructed. After this slope, distance and angle are calculated for all 1×60 features and getting a three feature vector of size 1×30 respectively. A new feature vector is constructed of size 1×90 and this vector is concatenated with an original vector of size 1×60 to get a final vector of size 1×150 . The slope, distance, and angle are calculated as shown below:

$$\text{Slope} = \frac{(V_{y_i} - V_{y_{i+1}})}{(V_{x_i} - V_{x_{i+1}})} \quad (34)$$

Where V_{y_i} represents the i th feature vector and $V_{y_{i+1}}$ represents the i th + 1 vector.

$$\text{Distance} = \sqrt{(V_{y_{i+1}} - V_{y_i})^2 + (V_{x_{i+1}} - V_{x_i})^2} \quad (35)$$

$$\text{Angle} = \tan^{-1}\left(\frac{V_{y_{i+1}} - V_{y_i}}{V_{x_{i+1}} - V_{x_i}}\right) \quad (36)$$

4.2 | Global features

The global features are utilized to describe the representation of the entire image. Many shapes and texture features fall in the category of global features. The global features are extracted to compute the edge's information of the entire image for the purpose of pattern recognition. In this phase, six global features are extracted name as aspect ratio, area, horizontal projection, vertical projection, pure height, and pure width. These features are extracted from the enhanced lesion image. It gives the feature vector of dimension 1×6 .

$$\text{AspectRatio} = \frac{W_d(x, y)}{H_t(x, y)} \quad (37)$$

$$\Delta = W_d(x, y) \times H_t(x, y) \quad (38)$$

$$H_p = \sum R_p(x) \quad (39)$$

$$V_p = \sum C_p(y) \quad (40)$$

$$\text{Height} = \max(V_p) \quad (41)$$

$$\text{Width} = \max(H_p) \quad (42)$$

Where, $W_d(x, y)$ denotes the width of lesion area, $H_t(x, y)$ denotes the height of lesion, Δ denotes the area, H_p and V_p denotes the horizontal projection and vertical projection, respectively.

4.3 | Shape features

Shape features are important for classification of lesion because the shape of each lesion is different as compared to other lesions. For this purpose, histogram oriented gradient (HOG) features (Alfed, Khelifi, & Bouridane, 2016) is extracted from the segmented lesion image. The vector dimension of segmented lesion region is $1 \times 236,880$. The dimension of extracted features is too high which affect the computation time. A principal component analysis (Shlens, 2014) algorithm is utilized for reduction of features dimension and getting a new vector of size $1 \times 2,368$ based on entropy value. The entropy is calculated

TABLE 2 Description of GLCM features

GLCM features	Equation
Auto correlation	$\widetilde{\varphi^R} = \sum_k \sum_l (k \times l) P(k, l)$
Contrast	$\widetilde{\varphi^C} = \sum_{k=1}^{\varphi^B} \sum_{l=1}^{\varphi^B} k - l ^2 P(k, l)$
Correlation 1	$\widetilde{\varphi^{R_1}} = \sum_{k=0}^{\varphi^B-1} \sum_{l=0}^{\varphi^B-1} (k \times l) P(k, l) - \varphi^{\mu_x} \varphi^{\mu_y}$
Correlation 2	$\widetilde{\varphi^{R_2}} = \frac{\sum_{k=0}^{\varphi^B-1} \sum_{l=0}^{\varphi^B-1} (k - \varphi^{\mu_k})(l - \varphi^{\mu_l}) P(k, l)}{\sigma}$
Cluster prominence	$\widetilde{\varphi^P} = \sum_{k=0}^{\varphi^B-1} \sum_{l=0}^{\varphi^B-1} \{k + 1 - \varphi^{\mu_x} - \varphi^{\mu_y}\}^4 P(k, l)$
Cluster shade	$\widetilde{\varphi^S} = \sum_{k=0}^{\varphi^B-1} \sum_{l=0}^{\varphi^B-1} \{k + 1 - \varphi^{\mu_x} - \varphi^{\mu_y}\}^3 P(k, l)$
Dissimilarity	$\widetilde{\varphi^D} = \sum_k \sum_l P(k, l) k - l $
Energy	$\widetilde{\varphi^E} = \sum_k \sum_l P(k, l)^2$
Entropy	$\widetilde{\varphi^H} = \sum_k \sum_l P(k, l) \log P(k, l)$
Homogeneity 1	$\widetilde{\varphi^{\alpha_1}} = \frac{\sum_{k=0}^{\varphi^B-1} \sum_{l=0}^{\varphi^B-1} P(k, l)}{1 + k - l }$
Homogeneity 2	$\widetilde{\varphi^{\alpha_2}} = \frac{\sum_{k=0}^{\varphi^B-1} \sum_{l=0}^{\varphi^B-1} P(k, l)}{1 + (k - l)^2}$
Maximum probability	$\widetilde{\varphi^P} = \max_k P(k, l)$
Sum of squares (variance)	$\widetilde{\varphi^{\sum \sigma^2}} = \sum_{k=1}^{\varphi^B-1} \sum_{l=1}^{\varphi^B-1} (k - \varphi^{\mu})^2 P(k, l)$
Sum average	$\widetilde{\varphi^{\sum A}} = \sum_{k=2}^{\varphi^B-2} k P_{x+y}(k)$
Sum entropy	$\widetilde{\varphi^{\sum H}} = - \sum_{k=2}^{\varphi^B-2} P_{x+y}(k) \log P_{k+1}(k)$
Sum variance	$\widetilde{\varphi^{\sum \sigma^2}} = - \sum_{k=2}^{\varphi^B-2} (k - \widetilde{\varphi^H}) P_{x+y}(k)$
Difference variance	$\widetilde{\varphi^{\sigma^2}} = \sigma^2(P_{x-y})$
Difference entropy	$\widetilde{\varphi^H} = - \sum_{k=0}^{\varphi^B-1} P_{k-l}(k) \log \{P_{k-l}(k)\}$
Information measure of correlation 1	$\widetilde{\varphi^M R_1} = \frac{\widetilde{\varphi^H} - H_{xy1}}{\max(H_x, H_y)}$
Information measure of correlation 2	$\widetilde{\varphi^M R_2} = \sqrt{(1 - \exp[-2.0(H_{xy2} - \widetilde{\varphi^H})])}$
Inverse difference normalized	$\widetilde{\varphi^{D^{-1}}} = \sum_k \sum_l \frac{P(k, l)}{1 + \frac{ k - l }{\varphi^B}}$
Inverse difference moment normalized	$\widetilde{\varphi^{D M^{-1}}} = \sum_k \sum_l \frac{P(k, l)}{1 + \frac{ k - l ^2}{\varphi^B}}$

for each feature set and select the higher entropy value 2,368 features for further process.

4.4 | Textural features

In this section, GLCM features (Haralick et al., 1973; Xu, Lu, Berendt, Jha, & Mandal, 2018) are obtained for the representation of lesion in the image. The GLCM features are extracted for the correct representation of a lesion into the category of melanoma and nonmelanoma. For this purpose, 22 GLCM features are extracted including entropy, homogeneity, variance, energy, and few more. The enhanced image is utilized for extraction of GLCM features and obtains a feature vector of dimension 1×22 . The brief description of GLCM features is shown in Table 2.

4.5 | Features integration and selection

In features integration phase, a simple but effective method is employed to integrate all set of features in one feature vector. The

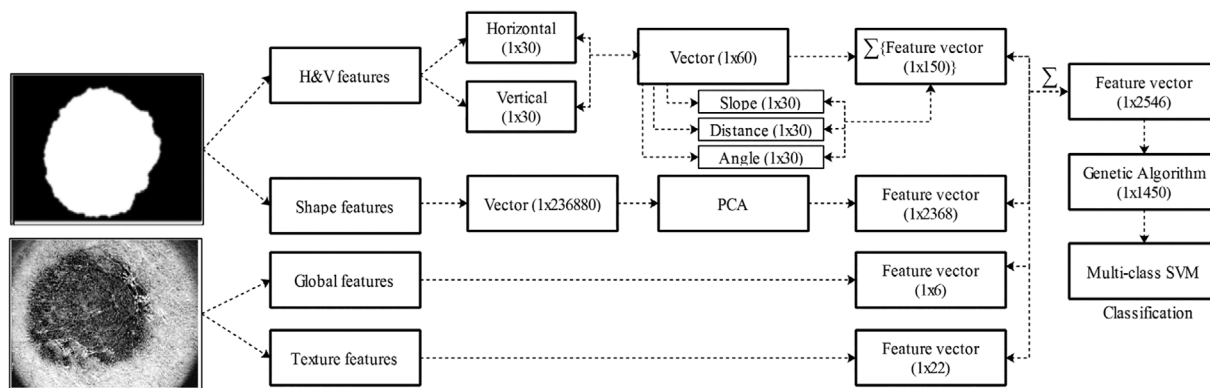


FIGURE 11 Complete model for features extraction, integration, and appropriate selection for classification

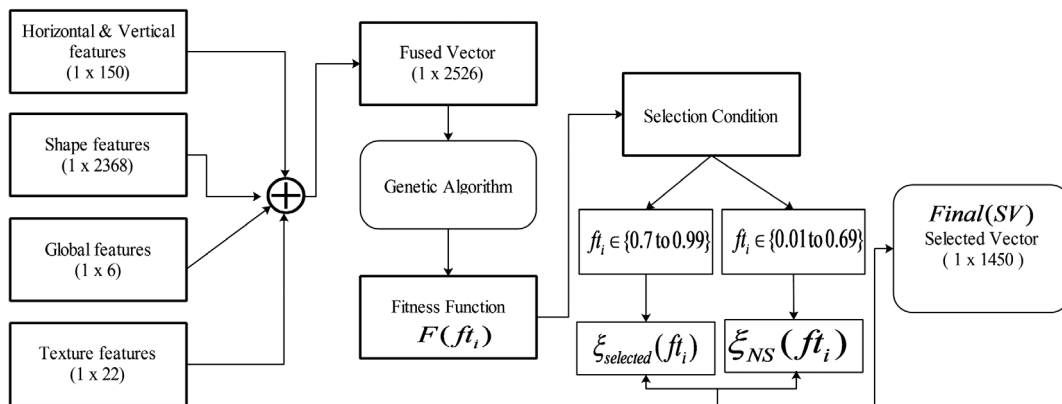


FIGURE 12 Architecture for features selection using GA

TABLE 3 Selected images for classification

Selected images for classification					
Dataset	Total images	Training images	Testing images	Cancer type # images	
				Bascall carcinoma	Atypical nevi
ISIC MSK-1	211	100	111	98	-
ISIC MSK-2	288	126	162	-	-
ISIC UDA-1	450	223	227	-	-
PH2	200	100	100	-	80
				80	80
					40

purpose of feature integration is to obtain a new feature vector, which consists of all information such as shape, global, texture. The extracted features are concatenated horizontally in the matrix, which

TABLE 4 ISIC-UDA-1-1 (benign vs melanoma)

Classifier	Accuracy measures					
	FPR	FNR (%)	TRP (%)	Prec (%)	FDR	Acc (%)
LR	0.10	11.0	0.88	88.65	11.35	89.0
F-KNN	0.12	13.20	0.86	86.40	13.6	86.8
W-KNN	0.09	9.7	0.90	89.95	10.05	90.3
DT	0.14	14.1	0.84	86.0	14.0	85.9
LDA	0.09	10.1	0.89	89.55	10.45	89.9
QDA	0.06	7.0	0.92	92.60	7.4	93.0
EBT	0.1	10.6	0.89	89.1	10.9	89.4
Proposed	0.05	6.2	0.93	93.5	6.5	93.8

defines as: Suppose the x_1, x_2, \dots, x_N are melanoma classes. Let $\ominus \in R^N$ is a trainingsample. As $\xi_{H/V}$, ξ_{HOG} , ξ_{GM} , ξ_{GLCM} are extracted set of features as H & V, HOG, global, and GLCM. The dimension of each extracted feature set is clear from Figure. 11. Then these features are fused given as:

$$FV(\xi_i) = \sum_{i=1}^L \psi(\xi_i), i \in 1, 2, 3, 4 \quad (43)$$

Where, L denotes the length of extracted vectors such as H/V, HOG, GM, and GLCM. The length of extracted vectors is (1×150) , (1×2368) , (1×6) , and (1×22) , respectively. Where $i = 1 - 4$ represents H/V, HOG, GM and GLCM features, respectively. Hence, the length of fithe nal fused vector is $(N1 \times 2546)$, where, $N1$ represents total number of dermoscopic images that are utilized for features extraction.

TABLE 5 Confusion matrix for ISIC-UDA-1-1 (benign vs melanoma) [Color table can be viewed at wileyonlinelibrary.com]

Class	Classification classes		TRP (%) FNR (%)
	Benign	Melanoma	
Benign	120	11	91.6 (%) 8.4 (%)
Melanoma	3	93	96.9 (%) 3.1 (%)

The final feature vector, $FV(\xi_i)$ is fed to a GA, whereas optimized features are the output which is given to the multi-class SVM. The major purpose of optimization is to select the most important features and remove the redundancy between them. The redundancy between features degrades the accuracy of the system and also increase the computation time. Recently, several features selection algorithms are introduced in the machine learning for selection of optimal features (Akram, Khan, Sharif, & Yasmin, 2018; Saptarshi Chatterjee et al., 2018; Khan et al., 2018; Khan, Akram, Sharif, Shahzad, et al., 2018; Liaqat et al., 2018; Nasir et al., 2018; Sharif, Khan, Faisal, Yasmin, & Fernandes, 2018; Sharif, Khan, Iqbal et al., 2018, Fotso et al., 2018a). GA is implemented for the selection of best features which is a combination of standard steps including a number of iteration, population initialization, crossover rate, mutation rate, selection pressure, and fitness function. Double point crossover (Man, Tang, & Kwong, 1996) has been used with mutation rate 0.4. The crossover is defined as:

$$Y_1 = \sum_{1}^{c_1} (p_1) \sum_{c_1+1}^{c_2} (p_2) \quad (44)$$

$$Y_2 = \sum_{1}^{c_1} (p_2) \sum_{c_1}^{c_2} (p_1) \quad (45)$$

Where p_1 and p_2 are selected parents, which are computed by Roulette Wheel selection (Lipowski & Lipowska, 2012) with selection pressure of six and c_1, c_2 are minimum and maximum randomsamples which are selected from a number of array elements. The number of arrayelements denotes the selected population size which is 100. Then, a uniform mutation (Juang, 2004) technique is implemented with the mutation rate of 0.3. Finally, a fitness function is computed as:

$$F(ft_i) = E \times (1 + (\beta \times \xi_{S_i})) \quad (46)$$

Where E is the mean of chromosomes and β is constant which is initialized to 0.5. Then selected the best features based of their highest fitness values as shown in the Figure 12.

TABLE 6 ISIC-MSK-1-1 (benign Vs Basall carcinoma)

Classifier	Accuracy measures					
	FPR	FNR (%)	TPR (%)	Prec (%)	FDR	Acc (%)
LR	0.02	1.8	0.98	98.4	1.6	98.2
F-KNN	0.10	10.8	0.89	89.1	10.9	89.2
W-KNN	0.11	11.7	0.88	88.2	11.7	88.3
DT	0.02	2.7	0.97	97.2	2.8	97.3
LDA	0.11	9.9	0.89	92.3	7.6	90.1
QDA	0.01	1.8	0.98	98.1	1.9	98.2
EBT	0.35	3.6	0.96	96.5	3.4	96.4
Proposed	0.01	0.9	0.99	99.2	0.8	99.1

TABLE 7 Confusion matrix ISIC-MSK-1-1 (benign vs Basall carcinoma) [Color table can be viewed at wileyonlinelibrary.com]

Class	Classification classes		TRP (%) FNR (%)
	Basall carcinoma	Benign	
Basall carcinoma	49	1	98.0 (%) 2.0 (%)
Benign	0	31	100 (%) 0.0 (%)

The highest fitness values are computed as:

$$Final(SV) = \begin{cases} \xi_{selected}(f_i) & \text{if } F(ft_i) \in \{0.7 \text{ to } 0.99\} \\ \xi_{N-S}(f_i) & \text{if } F(ft_i) \in \{0.01 \text{ to } 0.69\} \end{cases} \quad (47)$$

Where $\xi_{selected}(f_i)$ denotes the selected features having values between 0.7 to 0.99 and $\xi_{N-S}(f_i)$ is non selected features. Hence, a new selected feature vector $Final(SV)$ is constructed having a dimension of $1 \times 1,450$. Finally, the selected feature vector is fed to multi-class SVM for classification.

4.6 | Multi-class SVM

In this article, One-against-all method (Hsu & Lin, 2002) is utilized for the classification of melanoma classes. The kernel function of M-SVM is redial basis function (RBF), which provides better results compared to few other kernel functions including d such as linear kernel, Gaussian RBF, and polynomial kernel (Sangeetha & Kalpana, 2011). The RBF kernel is defined as:

$Kernel(f) = \exp(-\gamma \|x_i - x_j\|^2)$, where i, j denotes the number of extracted features. The M-SVM constructs ' K ' SVM models, where K represents the number of melanoma classes. The j th SVM is trained with the given melanoma samples having both positive and negative samples.

The given class $\Omega \in \{(x_1, y_1), (x_2, y_2), \dots, (x_n, y_n)\}$, where x_n denotes the image feature and $y_n \in \{1, -1\}$ denotes the class labels. It solves the following optimization problem as given below:

$$Cost = \min_{w^m, b^m, \zeta^m} \frac{1}{2} (w^m)^T w^m + C \sum_{i=1}^l \zeta_i^m \quad (48)$$

$$(w^m)^T \varphi(x_i) + b^m \leq -1 + \zeta_i^m, \text{ if } y_i = m, \\ \varphi(F) = \{F_x \in F_c : (|S| > |C|)\} \quad (49)$$

$$\cap(minPixels < |S| < maxPixels) \\ \cap(|S_{connected}| > |S| - \epsilon)\} \quad (50)$$

TABLE 8 ISIC-MSK-1-1 (benign vs Malanoma)

Classifier	Accuracy measures					
	FPR	FNR (%)	TPR (%)	Prec (%)	FDR	Acc (%)
LR	0.02	2.9	0.97	97.25	2.75	97.1
F-KNN	0.16	16.3	0.83	84.70	15.3	83.7
W-KNN	0.25	26.9	0.73	82.50	17.5	73.1
DT	0.03	3.8	0.96	96.20	3.8	96.2
LDA	0.05	5.8	0.94	94.85	5.1	94.2
QDA	0.06	6.7	0.93	93.3	6.7	93.3
EBT	0.03	2.9	0.97	97.1	2.9	97.1
Proposed	0.01	1.9	0.98	98.15	1.85	98.1

TABLE 9 Confusion matrix ISIC-MSK-1-1 (benign vs Melanoma)
[Color table can be viewed at wileyonlinelibrary.com]

Class	Classification classes		TRP (%) FNR (%)
	Melanoma	Benign	
Melanoma	28	2	96.2 (%) 3.8 (%)
Benign	0	31	100 (%) 0.0 (%)

TABLE 10 ISIC-MSK-2-1 (benign vs melanoma)

Classifier	Accuracy measures					
	FPR	FNR (%)	TPR (%)	Prec (%)	FDR	Acc (%)
LR	0.03	3.1	0.96	96.9	3.1	96.9
F-KNN	0.04	4.7	0.94	95.3	4.65	95.3
W-KNN	0.05	5.9	0.93	94.5	5.45	94.1
DT	0.03	3.1	0.96	96.85	3.1	96.9
LDA	0.02	2.4	0.97	97.6	2.3	97.6
QDA	0.03	3.5	0.96	96.45	3.55	96.5
EBT	0.02	2.8	0.97	97.2	2.8	97.2
Proposed	0.01	1.6	0.98	98.5	1.5	98.4

TABLE 11 Confusion matrix for ISIC-MSK-2-1 (benign vs melanoma)
[Color table can be viewed at wileyonlinelibrary.com]

Class	Classification classes		TRP (%) FNR (%)
	Benign	Melanoma	
Benign	80	2	98.4 (%) 1.6 (%)
Melanoma	2	78	98.5 (%) 1.5 (%)

where $\varphi(F)$ denotes the final function, (w^m) denotes the assigned weights, and Cost denotes the cost function.

5 | EXPERIMENTAL RESULTS AND DISCUSSION

The proposed system evaluated on three publically datasets such as ISIC, ISBI2016, and PH2. From ISIC dataset, three datasets are picked namely ISIC-MSK-1, ISIC-MSK-2, and ISIC-UDA-1. Each database consists of numbers of melanoma and benign images. The description of selected images is listed in Table 3. The selected benign lesions consist of common nevi, basal carcinoma, and atypical nevi. Cross-validation is set as 10 for validation of proposed system. The implemented model has been tested on seven classification methods such

TABLE 12 PH2 (common nevus vs melanoma)

Classifier	Accuracy measures					
	FPR	FNR (%)	TPR (%)	Prec (%)	FDR	Acc (%)
KNN	0.12	9.2	0.87	93.65	6.35	90.8
EBT	0.03	2.8	0.96	97.90	2.10	97.2
LDA	0.07	6.4	0.93	93.85	6.15	93.6
DT	0.04	4.6	0.95	94.90	5.10	95.4
Proposed	0.02	1.8	0.97	98.60	1.40	98.2

TABLE 13 Confusion matrix: PH2 (common nevus vs melanoma)
[Color table can be viewed at wileyonlinelibrary.com]

Class	Classification classes		TRP (%) FNR (%)
	Common Nevus	Melanoma	
Common Nevus	40	-	100 (%) 0.0 (%)
Melanoma	2	18	95.0 (%) 5.0 (%)

TABLE 14 PH2 database (atypical nevus vs melanoma)

Classifier	Accuracy measures					
	FPR	FNR (%)	TPR (%)	Prec (%)	FDR	Acc (%)
KNN	0.08	5.8	0.91	95.0	5.0	94.2
EBT	0.03	2.5	0.95	98.2	1.8	97.5
LDA	0.05	5.0	0.95	93.9	6.0	95.0
DT	0.09	9.2	0.90	89.2	10.7	90.8
Proposed	0.01	0.8	0.99	98.80	1.2	99.2

TABLE 15 Confusion matrix for PH2 database (atypical nevus vs melanoma) [Color table can be viewed at wileyonlinelibrary.com]

Class	Classification classes		TRP (%) FNR (%)
	Atypical nevus	Melanoma	
Atypical nevus	39	1	98.8 (%) 1.2 (%)
Melanoma	-	20	100 (%) 0.0 (%)

TABLE 16 PH2 database (atypical nevus vs common nevus vs melanoma)

Classifier	Accuracy measures					
	FPR	FNR (%)	TPR (%)	Prec (%)	FDR	Acc (%)
KNN	0.01	3.2	0.97	96.5	3.4	96.8
EBT	0.01	2.6	0.96	97.0	3.0	97.4
LDA	0.01	4.2	0.94	94.7	5.3	95.8
DT	0.02	6.3	0.92	92.4	7.5	93.7
Proposed	0.01	1.6	0.98	97.9	2.1	98.4

as logistic regression (LR), K-nearest neighbor (KNN), Weighted-KNN (W-KNN), decision tree (DT), LDA classifier, quadratic discriminant analysis (QDA) discriminant classifier, and ensemble boosted tree (EBT). The performance of classification models is validated by seven measures such as false negative rate (FNR), false positive rate (FPR), false directive rate (FDR), true positive rate (TPR), Precision (Prec), F1 score and accuracy (Acc). A comprehensive comparison has also been made with the existing classification techniques. The proposed model has been implemented on MATLAB 2018a using a personal desktop computer of 16GB RAM and 8 GB GPU.

5.1 | ISIC dataset

ISIC is an educational database, extensively used in skin cancer research (Gutman et al., 2016). It consists of a big number of open source high-quality dermoscopy images. It is used for clinicians and

TABLE 17 Confusion matrix for PH2 database (atypical nevus vs common Nevus vs melanoma) [Color table can be viewed at wileyonlinelibrary.com]

Classification class	Classification class			TPR (%) FNR (%)
	Atypical nevus	Common nevus	Melanoma	
Atypical nevus	38	0	2	97.5% 2.5%
Common nevus	-	40		100% 0.0%
Melanoma	-	1	19	97.5% 2.5%

TABLE 18 Proposed classification results on 4 datasets

Proposed results on 4 datasets using 7 performance measures						
FPR	FNR (%)	TPR	Precision (%)	FDR (%)	F1 score	Accuracy (%)
ISIC_MSK_1 (benign vs Bascall carcinoma)						
0.02	0.9	0.99	99.2	0.8	0.980	99.1
ISIC_MSK_1 (benign vs melanoma)						
0.01	1.9	0.98	98.15	1.85	0.981	98.1
ISIC_MSK_2 (benign vs melanoma)						
0.01	1.6	0.98	98.5	1.5	0.985	98.4
ISIC_UDA_1 (benign vs melanoma)						
0.05	6.2	0.93	93.5	6.5	0.932	93.8
PH2 (common nevus vs melanoma)						
0.02	1.8	0.97	98.60	1.40	0.980	98.2
PH2 (atypical nevus vs melanoma)						
0.01	0.8	0.99	98.80	1.20	0.993	99.2
PH2 (atypical nevus vs common nevus vs melanoma)						
0.01	1.6	0.98	97.90	2.10	0.979	98.4

educators to improve the diagnostics skills and provide an efficient solution for the identification of skin cancer. This dataset includes many sub-datasets in which we only selected three datasets as ISIC-UDA-1, ISIC-MSK-1, and ISIC-MSK-2 for classification.

5.1.1 | ISIC-UDA-1

ISIC-UDA-1 (Gutman et al., 2016) is a current dataset of ISIC industry. The dataset consists of 557 cutaneous melanotic lesions, which were collected from adults. For training and testing, a total of 450 images are selected, details are summarized in Table 3. To validate the proposed system, seven measures are undertaken as mentioned at the start of Section 5.

The classification results are given in Table 4 with achieved TPR of 91.6% for benign and 96.9% for the malignant melanoma, which are proved in Table 5. From Table 4 proposed model perform superior in term of TPR, precision rate, FPR, and accuracy. The proposed algorithm achieved an accuracy of 93.8%, TPR 93%, precision 93.5%, and FPR is 0.05, which is better than other classifiers. Moreover, the specificity is calculated for the proposed method results which obtained 91.3%. The specificity is calculated from Table 5.

5.1.2 | ISIC-MSK-1

This dataset consists of a single pigmented lesion clinic. It contains only those lesions, which are removed. Important clinic metadata such as analysis of gender age and clinical consequence of the lesion are included with each lesion image. It contains bascall carcinoma, benign, and melanoma (L. Yu et al., 2017). For training and testing phase, total 211 images are collected and training and testing description is presented in Table 3.

In Table 6, classification results are calculated among benign and bascall carcinoma. The best results are achieved 99.1% on M-SVM that are proved by confusion matrix (CM) in Table 7. From Table 8, shows the classification results of benign and melanoma and achieved the best accuracy 98.1% on proposed method, and proved by Table 9. Hence, from Tables 6 and 8, it is obvious that proposed algorithm outperforms on M-SVM as compare to other listed classifiers.

5.1.3 | ISIC-MSK-2

The ISIC-MSK-2 dataset (Gutman et al., 2016) consists of benign and melanoma images. The description of selected benign and melanoma

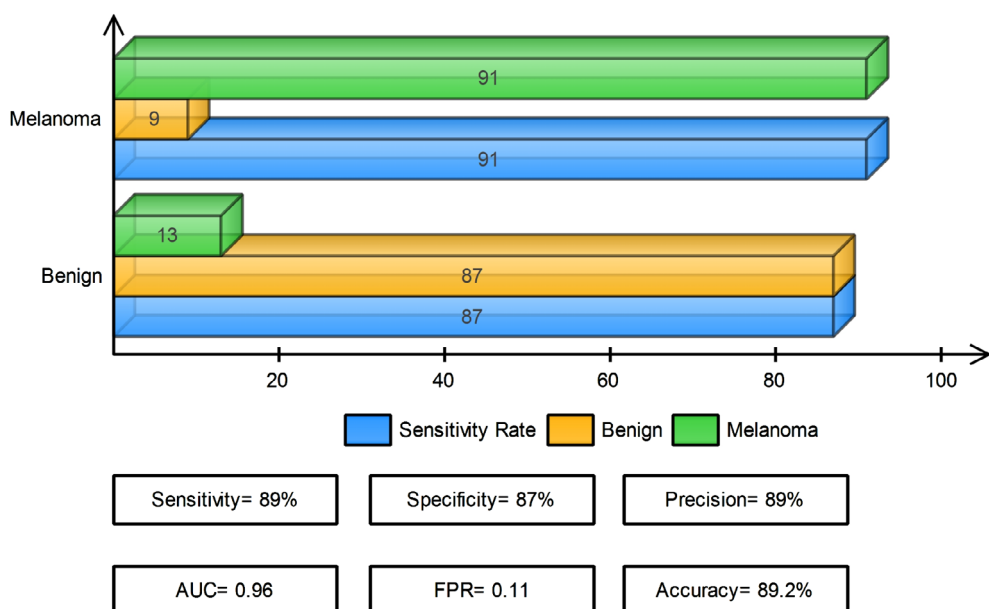


FIGURE 13 Recognition performance of proposed method on ISBI2016 dataset [Color figure can be viewed at wileyonlinelibrary.com]

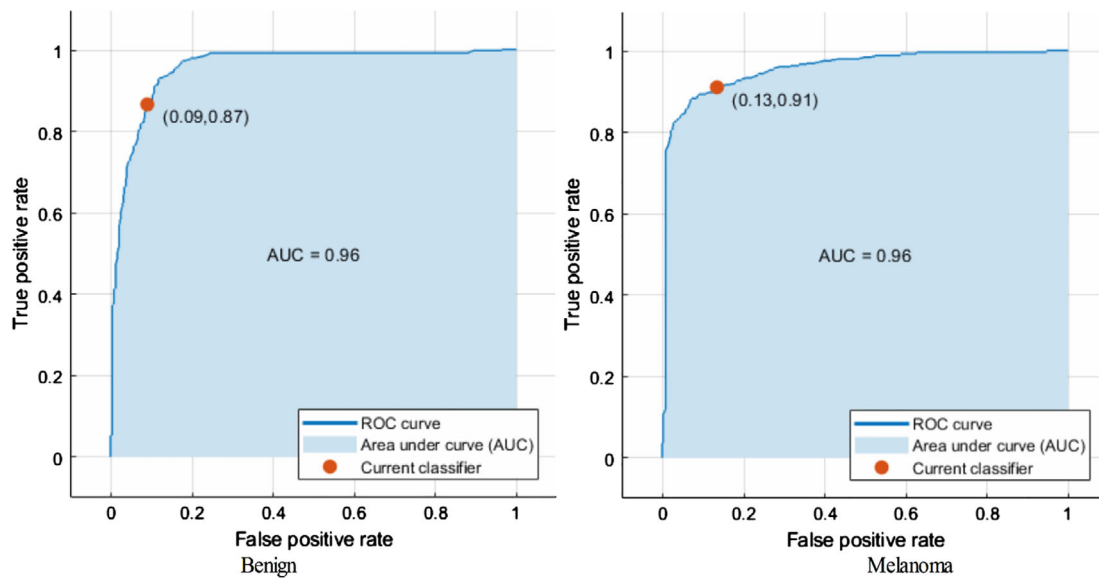


FIGURE 14 ROC results of proposed method on ISBIB2016 dataset [Color figure can be viewed at wileyonlinelibrary.com]

images for training & testing are depicted in Table 3. Proposed algorithm results are presented in Table 10, which are proved by their CM presented in Table 11. The Tables 10 and 11 confirms the authenticity and validity of our proposed techniques. From Table 10, achieved maximum accuracy of 98.4% on the proposed algorithm with TPR 0.98 and F1 score of 0.985.

5.2 | PH2 dataset

Ph2 database (Mendonça, Ferreira, Marques, Marcal, & Rozeira, 2013) consists of a total 200 dermoscopic images RGB images includes 80 common nevi, 80 atypical nevi, and 40 melanoma. All the images are 32 bites and having resolution 760×560 pixels. In Table 3, the number of training and testing samples are explained. The experiments have been carried out in three principal steps. First, experiments are done on common nevi and melanoma images and achieved maximum accuracy of 98.2% as presented in Table 12, and their CM in Table 13. In the second step, the experiment is done on

atypical nevi and melanoma. It achieved maximum accuracy 99.2% as shown in Table 14 and their confusion matrix in Table 15. In the third step, the experiment is done on all melanoma classes and achieved maximum accuracy of 98.4% as shown in Table 16 and confirmed by Table 17. From Tables 13, 15, and 16, it is clear that the proposed algorithm presents good performance as compared to other classification methods. To reveal the authenticity of the proposed algorithm, also calculated the TPR, precision, and F1 score, which is 0.98, 97.90, and 0.979 and also presented in Table 18.

5.3 | ISBI2016

The ISBI2016 dataset is a publicly available skin lesion dataset. This dataset is a variety of superiority controlled RGB images. It consists of total 1,279 dermoscopic images includes 273 malignant and 1,006 benign. It includes 900 training images from 1,279 and 350 testing RGB images of many sizes. To evaluate performance of proposed

TABLE 19 Comparison with recent methods for PH2 dataset. These results are just compared with PH2 dataset

Method	Year	TPR (%)	Specificity (%)	Accuracy (%)	F1 score
(C. Barata, Celebi, & Marques, 2015)	2015	92.5	76.3	84.3	-
(Wu et al., 2018)	2015	90.0	90	-	-
(Rastgoo, Morel, Marzani, & Garcia, 2015)	2015	94.0	92	-	-
(Rastgoo et al., 2016)	2016	92.5	81.7	-	-
(Bi, Kim, Ahn, Feng, & Fulham, 2016)	2016	87.5	93.13	92.0	-
(Chakravorty, Liang, Abedini, & Garnavi, 2016)	2016	81.0	90.0	83.0	90.0
(Satheesha et al., 2017)	2017	93.0	97.0	-	-
(Nasir et al., 2018)	2018	97.7	96.7	97.5	97.5
(Akram et al., 2018)	2018	96.3	99.5	97.5	-
Proposed	2017	98.0	98.75	98.4	97.9

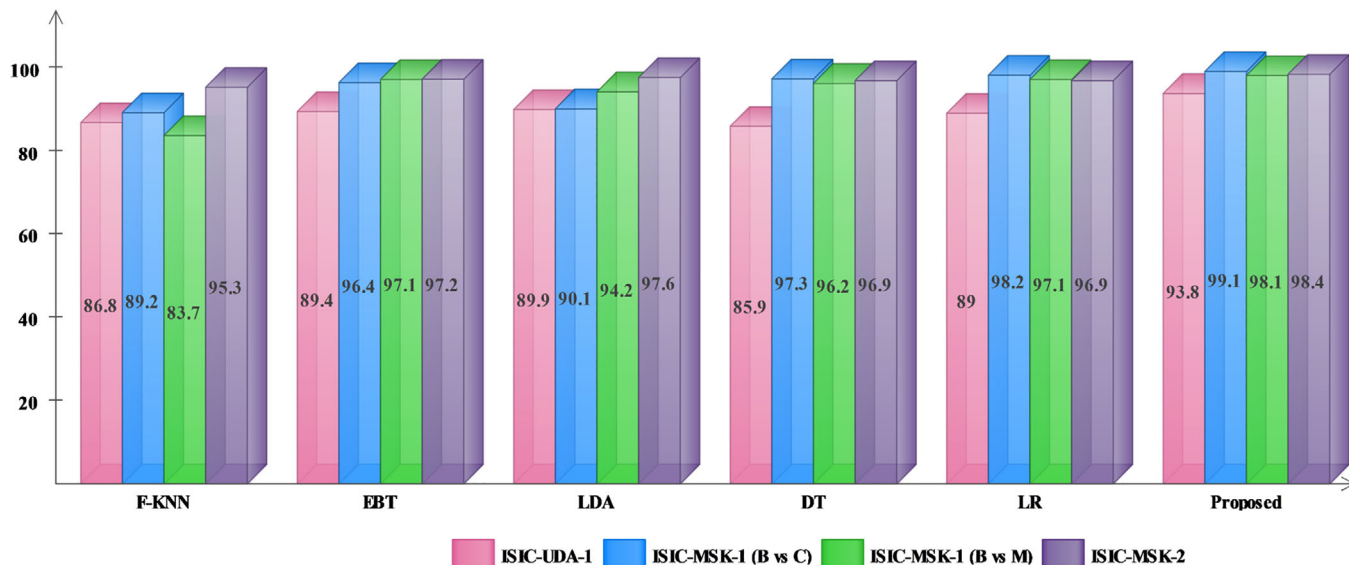


FIGURE 15 Comparison results of ISIC dataset with different classification methods in terms of accuracy. C denotes the Basal carcinoma, B denotes the benign and M denotes the melanoma [Color figure can be viewed at wileyonlinelibrary.com]

system, 50:50 approach is opted and validate through of 10-fold. The achieved classification performance such on ISBI2016 such as accuracy, specificity, sensitivity, precision rate, AUC, and FPR is 89.2, 87, 89, 89, 0.96, and 0.11, respectively. The classification results of ISBI2016 are shown in Figures 13 and 14, which shows the system authenticity. The proposed system performance is also conducted with few recent methods such as (Ge et al., 2017) and (Lopez, Giro-i-Nieto, Burdick, & Marques, 2017). In (Ge et al., 2017) achieved classification accuracy is 85.0% using ISBI 2016 datasets, whereas in (Lopez et al., 2017), the reported accuracy is 81.33% for ISBI 2016 dataset. But the proposed

approach reached up to 89.2%, which is better as compare to (Ge et al., 2017) and (Lopez et al., 2017).

6 | DISCUSSION

We summarize our system in this section in terms of both qualitative and quantitative results. The proposed algorithm implement for accurate melanoma segmentation and classification. Six principle steps are performed for this system which starts from preprocessing and end from classification. Each step is an amalgamation of

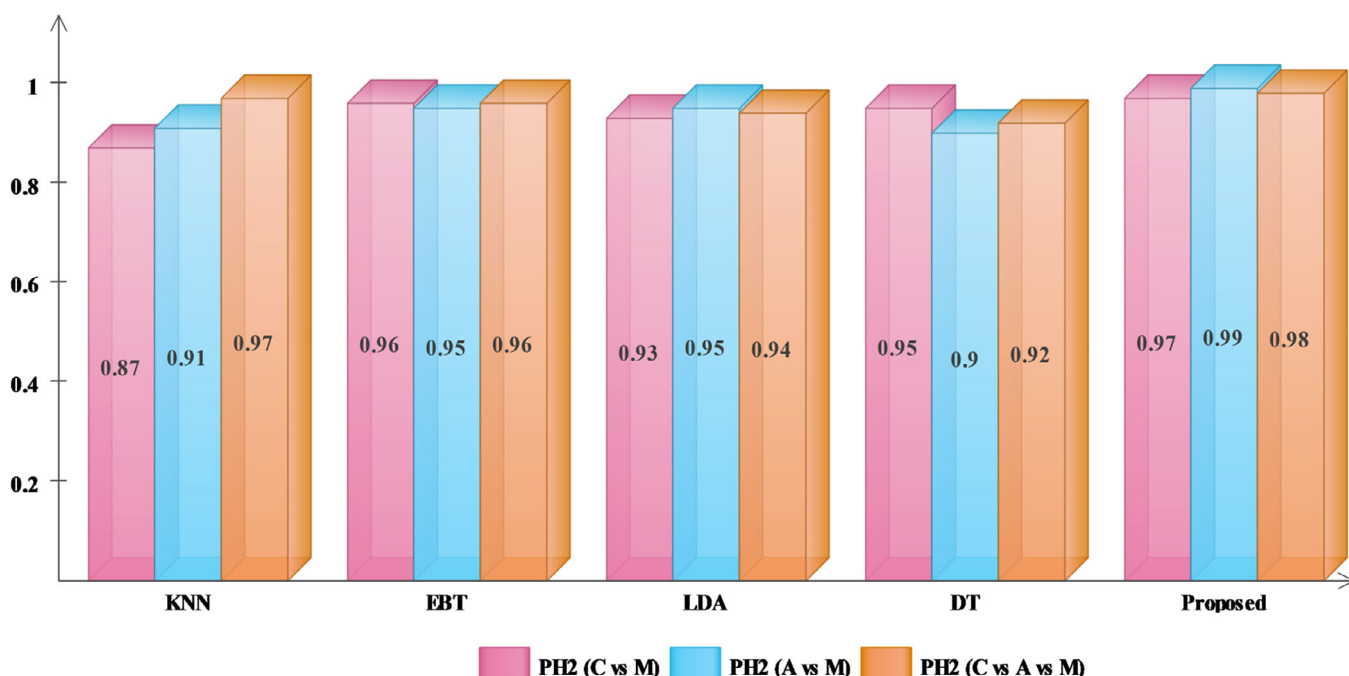


FIGURE 16 Comparison results on PH2 dataset with different classification methods in terms of TPR. A denotes the atypical melanoma and M denotes the melanoma [Color figure can be viewed at wileyonlinelibrary.com]

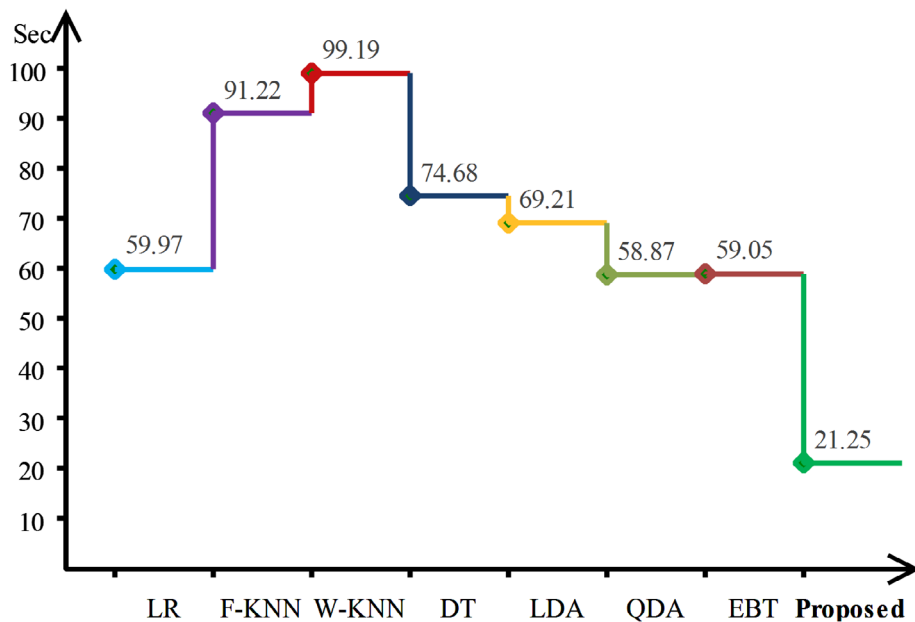


FIGURE 17 Classification time for ISIC UDA-1 dataset [Color figure can be viewed at wileyonlinelibrary.com]

substeps as shown in Figure 2. The segmentation results with their corresponding ground truth image are shown in Figure 10. The segmentation accuracy results are presented in Table 1 and Table 1-A. For classification of melanoma, three publically available datasets are selected. Four types of feature are extracted as depicted in Section 4. The extracted features are integrated based on their vector dimension and then selected discriminative features based on GA as shown in Figure 11. The proposed results compared with five general classification algorithms such as KNN, EBT, LDA, DT, and LR on selected datasets as shown in Tables 5, 7, 9, 11, 13, 15, and 16 which is confirms by their CM in Tables 6, 8, 10, 12, 14, 16, and 17. Moreover, the performance of ISBI2016 dataset is given in

Figures 13 and 14. The overall classification results for selected datasets are shown in Table 18, and their comparison with existing techniques is shown in Table 19. The proposed results compared with existing methods confirm the superiority of implemented system. The comparison results in Table 19 compared with results of the PH2 dataset in terms of TPR, specificity, accuracy, and F1 measures. Also, the graphical results are plotted in Figures 15 and 16. Also, the classification performance of proposed algorithm on ISBI2016 dataset is compared with two latest methods. Ge et al. (2017) introduced a generic features based approach, whereas in Lopez et al. (Lopez et al., 2017) introduced deep learning method for skin lesion classification. The proposed achieved accuracy on

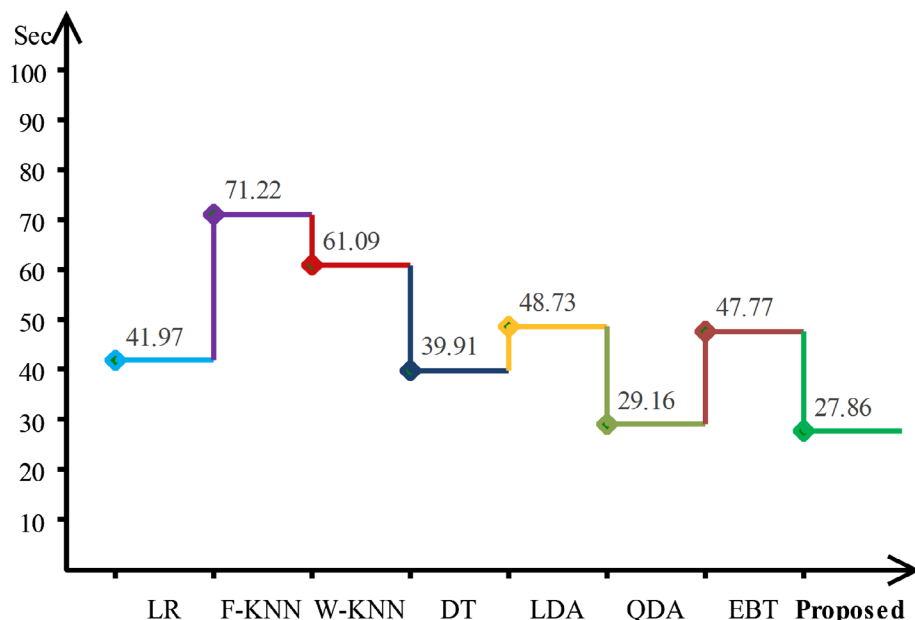


FIGURE 18 Classification time for ISIC MSK-1 dataset [Color figure can be viewed at wileyonlinelibrary.com]

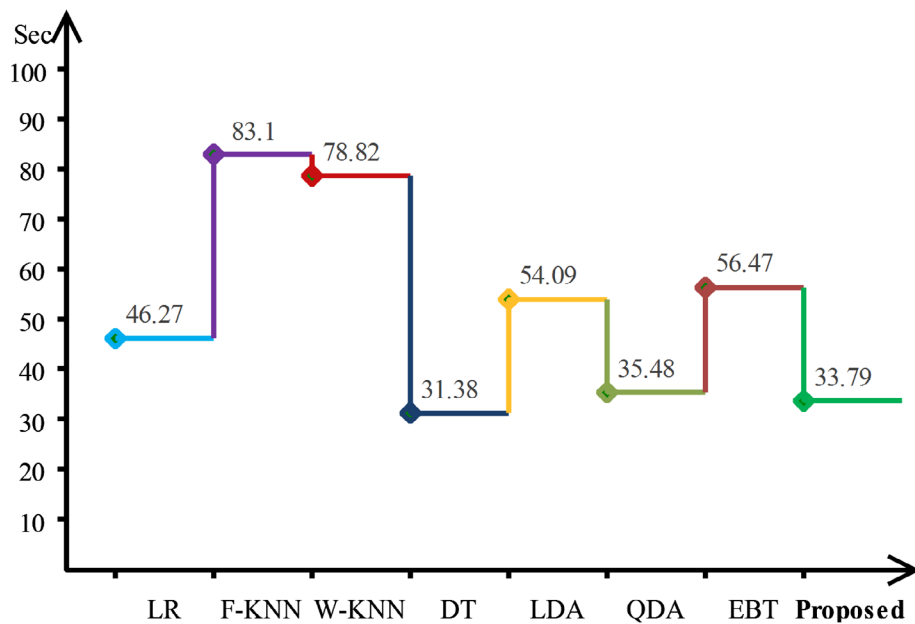


FIGURE 19 Classification time for ISIC MSK-2 dataset [Color figure can be viewed at wileyonlinelibrary.com]

ISBI 2016 is 89.2% which is superior as compared to mentioned techniques. In addition, the classification execution time of proposed method on ISBI 2016 dataset is 41.937 seconds.

In addition, the classification time for ISIC-UDA-1, ISIC MSK-1, ISIC-MSK-2, and PH2 are calculated and plotted in Figures 17–19, and 20. In Figure 17, the best-obtained classification time is 21.25 s for the proposed approach. The second best-achieved classification time is 58.87 s on QDA classifier. Similarly, in Figures 18–19, and 20 the best classification time is 27.86 s, 33.79 s, and 29.76 s, respectively for proposed method. The execution time of F-KNN is higher than other classifiers for all datasets, whereas the proposed system performs superior.

7 | CONCLUSION

An automated system for skin lesion detection and classification is proposed in this work. The proposed technique is split into two phases: in the first phase, mean of the top-bottom filtering image is calculated, followed by log transformation to enhance the contrast of lesion regions. We have demonstrated that this contrast enhancement leads to improved segmentation results. In the second phase, four types of features are extracted, and GA is utilized for prominent features selection by SVM. The experiments are conducted using three publicly available datasets, PH2, ISBI2016, and ISIC, and the results have shown an improved performance.

In future, the same algorithm is implemented on ISBI 2017 and ISBI2018 skin datasets using deep features (Chen, Shi, et al., 2017). In computer vision, the deep learning method performs efficiently well when we have a large number of the dataset. Therefore, the existing methods such as texture features, shape features, and color features are suitable for large datasets. The major advantage of deep features is that it can efficiently work on big data and also improved the computation problem (Zhang et al., 2017).

DECLARATION

- **Ethics approval and consent to participate:**
Not applicable
- **Consent for publication:**
Not applicable
- **Availability of data and material:**
The datasets analysed during the current study are in open access using the following links.
 1. AADI project repository at the web link: <https://www.fc.up.pt/addi/ph2>
 2. ISIC UDA archive. <https://isic-archive.com/>

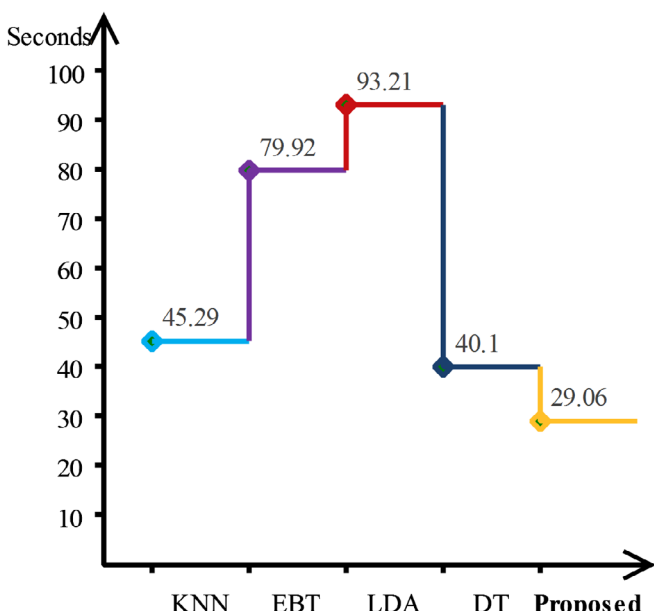


FIGURE 20 Classification time for PH2 dataset [Color figure can be viewed at wileyonlinelibrary.com]

- **Competing interests:** The authors declare that they have no competing interests.

ACKNOWLEDGMENT

This work is supported by the Machine Learning Research Group; Prince Sultan University Riyadh; Saudi Arabia [RG-CCIS-2017-06-02]; The authors are grateful for this support.

ORCID

Tanzila Saba  <https://orcid.org/0000-0003-3138-3801>

REFERENCES

- Abbas, N., Saba, T., Mohamad, D., Rehman, A., Almazyad, A. S., & Al-Ghamdi, J. S. (2016). Machine aided malaria parasitemia detection in Giemsa-stained thin blood smears. *Neural Computing and Applications*, 29(3), 803–818. <https://doi.org/10.1007/s00521-016-2474-6>
- Abbas, N., Saba, T., Rehman, A., Mehmood, Z., Kolivand, H., Uddin, M., & Anjum, A. (2018). Plasmodium life cycle stage classification based quantification of malaria parasitaemia in thin blood smears. *Microscopy Research and Technique*. <https://doi.org/10.1002/jemt.23170>
- Agarwal, A., Issac, A., Dutta, M. K., Riha, K., & Uher, V. (2017). Automated skin lesion segmentation using K-Means clustering from digital dermoscopic images. Paper presented at the Telecommunications and Signal Processing (TSP), 2017 40th International Conference.
- Akram, T., Khan, M. A., Sharif, M., & Yasmin, M. (2018). Skin lesion segmentation and recognition using multichannel saliency estimation and M-SVM on selected serially fused features. *Journal of Ambient Intelligence and Humanized Computing*, 1–20.
- Alfed, N., Khelifi, F., & Bouridane, A. (2016). Improving a bag of words approach for skin cancer detection in dermoscopic images. Paper presented at the Control, Decision and Information Technologies (CoDIT), 2016 International Conference.
- Altekrule, S., Kosary, C., Krapcho, M., Neyman, N., Aminou, R., Waldron, W., ... Cho, H. (2010). SEER Cancer statistics review, 1975–2007. Bethesda, MD: National Cancer Institute Blagosklonny MV and Campisi J. Cancer and aging: more puzzles, more promises, 2010:2615–2618.
- Argenziano, G., Fabbrocini, G., Carli, P., De Giorgi, V., Sammarco, E., & Delfino, M. (1998). Epiluminescence microscopy for the diagnosis of doubtful melanocytic skin lesions: Comparison of the ABCD rule of dermatoscopy and a new 7-point checklist based on pattern analysis. *Archives of Dermatology*, 134(12), 1563–1570.
- Baldwin, L., & Dunn, J. (2013). Global controversies and advances in skin cancer. *Asian Pacific Journal of Cancer Prevention*, 14(4), 2155–2157.
- Barata, A. C. F. (2017). Automatic detection of melanomas using dermoscopy images. Instituto Superior Tecnico.
- Barata, C., Celebi, M. E., & Marques, J. S. (2015). Improving dermoscopy image classification using color constancy. *IEEE Journal of Biomedical and Health Informatics*, 19(3), 1146–1152.
- Barata, C., Ruela, M., Francisco, M., Mendonça, T., & Marques, J. S. (2014). Two systems for the detection of melanomas in dermoscopy images using texture and color features. *IEEE Systems Journal*, 8(3), 965–979.
- Bi, L., Kim, J., Ahn, E., Feng, D., & Fulham, M. J. (2016). Automatic melanoma detection via multi-scale lesion-biased representation and joint reverse classification. Paper presented at the ISBI.
- Cancer Facts & Figures 2017 Cancer Statistics 2017, a scientific paper published in the American Cancer Society journal, CA: A Cancer Journal for Clinicians. <https://www.cancer.org/content/cancer/en/research/cancer-facts-statistics/all-cancer-facts-figures/cancer-facts-figures-2017.html>.
- Chakravorty, R., Liang, S., Abedini, M., & Garnavi, R. (2016). Dermatologist-like feature extraction from skin lesion for improved asymmetry classification in PH 2 database. Paper presented at the Engineering in Medicine and Biology Society (EMBC), 2016 I.E. 38th Annual International Conference
- Chander, A., Chatterjee, A., & Siarry, P. (2011). A new social and momentum component adaptive PSO algorithm for image segmentation. *Expert Systems with Applications*, 38(5), 4998–5004.
- Chatterjee, S., Dey, D., & Munshi, S. (2017). Development of a superpixel based local color feature extraction technique for the classification of skin lesions. Paper presented at the Calcutta Conference (CALCON), 2017 IEEE.
- Chatterjee, S., Dey, D., & Munshi, S. (2018). Optimal selection of features using wavelet fractal descriptors and automatic correlation bias reduction for classifying skin lesions. *Biomedical Signal Processing and Control*, 40, 252–262.
- Chen, M., Ma, Y., Li, Y., Wu, D., Zhang, Y., & Youn, C.-H. (2017). Wearable 2.0: Enabling human-cloud integration in next generation healthcare systems. *IEEE Communications Magazine*, 55(1), 54–61.
- Chen, M., Ma, Y., Song, J., Lai, C.-F., & Hu, B. (2016). Smart clothing: Connecting human with clouds and big data for sustainable health monitoring. *Mobile Networks and Applications*, 21(5), 825–845.
- Chen, M., Shi, X., Zhang, Y., Wu, D., & Guizani, M. (2017). Deep features learning for medical image analysis with convolutional autoencoder neural network. *IEEE Transactions on Big Data*, (1), 1–1.
- Fahad, H. M., Ghani Khan, M. U., Saba, T., Rehman, A., & Iqbal, S. (2018). Microscopic abnormality classification of cardiac murmurs using ANFIS and HMM. *Microscopy Research and Technique*, 81(5), 449–457. <https://doi.org/10.1002/jemt.22998>
- Fan, H., Xie, F., Li, Y., Jiang, Z., & Liu, J. (2017). Automatic segmentation of dermoscopy images using saliency combined with Otsu threshold. *Computers in Biology and Medicine*, 85, 75–85.
- Fidler, M. M., Gupta, S., Soerjomataram, I., Ferlay, J., Steliarova-Foucher, E., & Bray, F. (2017). Cancer incidence and mortality among young adults aged 20–39 years worldwide in 2012: A population-based study. *The Lancet Oncology*, 18(12), 1579–1589.
- Flores, E., & Scharcanski, J. (2016). Segmentation of melanocytic skin lesions using feature learning and dictionaries. *Expert Systems with Applications*, 56, 300–309.
- Fonseca-Pinto, R., & Machado, M. (2017). A textured scale-based approach to melanocytic skin lesions in dermoscopy. Paper presented at the Information and Communication Technology, Electronics and Microelectronics (MIPRO), 2017 40th International Convention.
- Fotso, K. G. A., Akram, T., Bitjoka, L., Syed, R. N., Mengue, M. A., & Nazeer, M. (2018a). A deep heterogeneous heterogeneous feature fusion approach for automatic land-use classification. *Information Sciences*, 467, 199–218.
- Ge, Z., Demyanov, S., Bozorgtabar, B., Abedini, M., Chakravorty, R., Bowling, A., & Garnavi, R. (2017). Exploiting local and generic features for accurate skin lesions classification using clinical and dermoscopy imaging. Paper presented at the Biomedical Imaging (ISBI 2017), 2017 I.E. 14th International Symposium.
- Glaister, J., Wong, A., & Clausi, D. A. (2014). Segmentation of skin lesions from digital images using joint statistical texture distinctiveness. *IEEE Transactions on Biomedical Engineering*, 61(4), 1220–1230.
- Gutman, D., Codella, N. C., Celebi, E., Helba, B., Marchetti, M., Mishra, N., & Halpern, A. (2016). Skin lesion analysis toward melanoma detection: A challenge at the international symposium on biomedical imaging (ISBI) 2016, hosted by the international skin imaging collaboration (ISIC). *arXiv preprint arXiv:1605.01397*.
- Haralick, R. M., Shanmugam, K., & Dinstein, I. H. (1973). Textural features for image classification. *IEEE Transactions on Systems, Man, and Cybernetics*, 3(6), 610–621.
- Hsiao, S. W., Yen, C. H., & Lee, C. H. (2017). An intelligent skin-color capture method based on fuzzy C-means with applications. *Color Research & Application*, 42(6), 775–787.
- Hsu, C.-W., & Lin, C.-J. (2002). A comparison of methods for multiclass support vector machines. *IEEE Transactions on Neural Networks*, 13(2), 415–425.
- Husham, A., Alkawaz, M. H., Saba, T., Rehman, A., & Alghamdi, J. S. (2016). Automated nuclei segmentation of malignant using level sets. *Microscopy Research and Technique*, 79(10), 993–997. <https://doi.org/10.1002/jemt.22733>
- Iqbal, S., Ghani, M. U., Saba, T., & Rehman, A. (2018). Brain tumor segmentation in multi-spectral MRI using convolutional neural networks

- (CNN). *Microscopy Research and Technique*, 81(4), 419–427. <https://doi.org/10.1002/jemt.22994>
- Iqbal, S., Khan, M. U. G., Saba, T., & Rehman, A. (2017). Computer assisted brain tumor type discrimination using magnetic resonance imaging features. *Biomedical Engineering Letters*, 8(1), 5–28. <https://doi.org/10.1007/s13534-017-0050-3>
- Jamal, A., Hazim Alkawaz, M., Rehman, A., & Saba, T. (2017). Retinal imaging analysis based on vessel detection. *Microscopy Research and Technique*, 80(17), 799–811. <https://doi.org/10.1002/jemt>
- Jerant, A. F., Johnson, J. T., Demastes Sheridan, C., & Caffrey, T. J. (2000). Early detection and treatment of skin cancer. *American Family Physician*, 62(2).
- Juang, C.-F. (2004). A hybrid of genetic algorithm and particle swarm optimization for recurrent network design. *IEEE Transactions on Systems, Man, and Cybernetics, Part B (Cybernetics)*, 34(2), 997–1006.
- Kasmi, R., & Mokrani, K. (2016). Classification of malignant melanoma and benign skin lesions: Implementation of automatic ABCD rule. *IET Image Processing*, 10(6), 448–455.
- Khan, M. A., Akram, T., Sharif, M., Javed, M. Y., Muhammad, N., & Yasmin, M. (2018). An implementation of optimized framework for action classification using multilayers neural network on selected fused features. *Pattern Analysis and Applications*, 1–21.
- Khan, M. A., Akram, T., Sharif, M., Shahzad, A., Aurangzeb, K., Alhussein, M., ... Altamrah, A. (2018). An implementation of normal distribution based segmentation and entropy controlled features selection for skin lesion detection and classification. *BMC Cancer*, 18(1), 638.
- Kiani, K., & Sharafat, A. R. (2011). E-shaver: An improved DullRazor® for digitally removing dark and light-colored hairs in dermoscopic images. *Computers in Biology and Medicine*, 41(3), 139–145.
- Kimball, T. G. (2018). Is Cancer A Moral Failing? What About Addiction? Why cancer treatment protocols can help destigmatize addiction and improve outcomes. *Young*.
- Lee, T., Ng, V., Gallagher, R., Coldman, A., & McLean, D. (1997). Dullrazor®: A software approach to hair removal from images. *Computers in Biology and Medicine*, 27(6), 533–543.
- Liaqat, A., Khan, M. A., Shah, J. H., Sharif, M., Yasmin, M., & Fernandes, S. L. (2018). Automated ulcer and bleeding classification from WCE images using multiple features fusion and selection. *Journal of Mechanics in Medicine and Biology*, 1850038.
- Lin, B. S., Michael, K., Kalra, S., & Tizhoosh, H. (2017). Skin lesion segmentation: U-Nets versus clustering. Paper presented at the Computational Intelligence (SSCI), 2017 I.E. Symposium Series.
- Lipowski, A., & Lipowska, D. (2012). Roulette-wheel selection via stochastic acceptance. *Physica a: Statistical Mechanics and its Applications*, 391 (6), 2193–2196.
- Lopez, A. R., Giro-i-Nieto, X., Burdick, J., & Marques, O. (2017). Skin lesion classification from dermoscopic images using deep learning techniques. Paper presented at the Biomedical Engineering (BioMed), 2017 13th IASTED International Conference.
- Mahbod, A., Ecker, R., & Ellinger, I. (2017). Skin Lesion Classification Using Hybrid Deep Neural Networks. arXiv preprint arXiv:1702.08434.
- Majtnner, T., Lidayova, K., Yildirim-Yayiglan, S., & Hardeberg, J. Y. (2016). Improving skin lesion segmentation in dermoscopic images by thin artefacts removal methods. Paper presented at the Visual Information Processing (EUVIP), 2016 6th European Workshop.
- Man, K.-F., Tang, K.-S., & Kwong, S. (1996). Genetic algorithms: Concepts and applications [in engineering design]. *IEEE Transactions on Industrial Electronics*, 43(5), 519–534.
- Markovic, S. N., Erickson, L. A., Rao, R. D., McWilliams, R. R., Kottschade, L. A., Creagan, E. T., ... Pockaj, B. A. (2007). Malignant melanoma in the 21st century, part 1: Epidemiology, risk factors, screening, prevention, and diagnosis. Paper presented at the Mayo Clinic Proceedings.
- Masood, A., & Al-Jumaily, A. A. (2013). Fuzzy C mean thresholding based level set for automated segmentation of skin lesions. *Journal of Signal and Information Processing*, 4(03), 66–71.
- Mayer, J. (1997). Systematic review of the diagnostic accuracy of dermatoscopy in detecting malignant melanoma. *Medical Journal of Australia*, 167(4), 206–210.
- Melanoma skin cancer in Australia. (2017). <https://melanoma.canceraustralia.gov.au/statistics>.
- Mendonça, T., Ferreira, P. M., Marques, J. S., Marcal, A. R., & Rozeira, J. (2013). PH 2-A dermoscopic image database for research and benchmarking. Paper presented at the Engineering in Medicine and Biology Society (EMBC), 2013 35th Annual International Conference of the IEEE.
- Menzies, S. W., Ingvar, C., Crotty, K. A., & McCarthy, W. H. (1996). Frequency and morphologic characteristics of invasive melanomas lacking specific surface microscopic features. *Archives of Dermatology*, 132(10), 1178–1182.
- Mirzaalian, H., Lee, T. K., & Hamarneh, G. (2014). Hair enhancement in dermoscopic images using dual-channel quaternion tubularness filters and MRF-based multilabel optimization. *IEEE Transactions on Image Processing*, 23(12), 5486–5496.
- Mohamed, A. A. I., Ali, M. M., Nusrat, K., Rahebi, J., Sayiner, A., & Kandemirli, F. (2017). Melanoma skin cancer segmentation with image region growing based on fuzzy clustering mean. *International Journal of Engineering Innovation & Research*, 6(2), 2277–5668.
- Mughal, B., Muhammad, N., Sharif, M., Rehman, A., & Saba, T. (2018). Removal of pectoral muscle based on topographic map and shape-shifting silhouette. *BMC Cancer*, 18, 778. <https://doi.org/10.1186/s12885-018-4638-5>
- Mughal, B., Muhammad, N., Sharif, M., Saba, T., & Rehman, A. (2017a). Extraction of breast border and removal of pectoral muscle in wavelet domain. *Biomedical Research*, 28(11), 5041–5043.
- Mughal, B., Muhammad, N., Sharif, M., Saba, T., & Rehman, A. (2017c). Extraction of breast border and removal of pectoral muscle in wavelet domain. *Biomedical Research*, 28(11), 5041–5043.
- Mughal, B., Sharif, M., Muhammad, N., & Saba, T. (2017). A novel classification scheme to decline the mortality rate among women due to breast tumor. *Microscopy Research and Technique*, 81, 171–180. <https://doi.org/10.1002/jemt.22961>
- Nachbar, F., Stoltz, W., Merkle, T., Cognetta, A. B., Vogt, T., Landthaler, M., ... Plewig, G. (1994). The ABCD rule of dermatoscopy: High prospective value in the diagnosis of doubtful melanocytic skin lesions. *Journal of the American Academy of Dermatology*, 30(4), 551–559.
- Nasir, M., Attique Khan, M., Sharif, M., Lali, I. U., Saba, T., & Iqbal, T. (2018). An improved strategy for skin lesion detection and classification using uniform segmentation and feature selection based approach. *Microscopy Research and Technique*, 81, 528–543.
- Norouzi, A., Rahim, M. S. M., Altameem, A., Saba, T., Rada, A. E., Rehman, A., & Uddin, M. (2014). Medical image segmentation methods, algorithms, and applications. *IETE Technical Review*, 31(3), 199–213. <https://doi.org/10.1080/02564602.2014.906861>
- Papamichail, M., Nikolaidis, I., Nikolaidis, N., Glava, C., Lentzas, I., Marmagkiolis, K., ... Digalakis, M. (2008). Merkel cell carcinoma of the upper extremity: Case report and an update. *World Journal of Surgical Oncology*, 6(1), 32.
- Rahman, M., Alpaslan, N., & Bhattacharya, P. (2016). Developing a retrieval based diagnostic aid for automated melanoma recognition of dermoscopic images. Paper presented at the 2016 I.E. Applied Imagery Pattern Recognition Workshop (AIPR).
- Rastgoo, M., Lemaitre, G., Massich, J., Morel, O., Marzani, F., Garcia, R., & Meriaudeau, F. (2016). Tackling the problem of data imbalancing for melanoma classification. Paper presented at the Bioimaging.
- Rastgoo, M., Morel, O., Marzani, F., & Garcia, R. (2015). Ensemble approach for differentiation of malignant melanoma. Paper presented at the Twelfth International Conference on Quality Control by Artificial Vision 2015.
- Rehman, A., Abbas, N., Saba, T., Ijaz ur Rahman, S., Mahmood, Z., & Kolivand, K. (2018). Classification of acute lymphoblastic leukemia using deep learning. *Microscopy Research & Technique*, 81, 1310–1317. <https://doi.org/10.1002/jemt.23139>
- Rehman, A., Abbas, N., Saba, T., Mahmood, T., & Kolivand, H. (2018). Rouleaux red blood cells splitting in microscopic thin blood smear images via local maxima, circles drawing, and mapping with original RBCs. *Microscopic Research and Technique*, 81(7), 737–744. <https://doi.org/10.1002/jemt.23030>
- Rehman, A., Abbas, N., Saba, T., Mahmood, Z., Mahmood, T., & Ahmed, K. T. (2018). Microscopic malaria parasitemia diagnosis and grading on benchmark datasets. *Microscopic Research and Technique*. <https://doi.org/10.1002/jemt.23071>

- Saba, T., Bokhari, S. T. F., Sharif, M., Yasmin, M., & Raza, M. (2018). Fundus image classification methods for the detection of glaucoma: A review. *Microscopy Research and Technique*, 81, 1105–1121. <https://doi.org/10.1002/jemt.23094>
- Saba, T., Rehman, A., Mehmood, Z., Kolivand, H., & Sharif, M. (2018). Image enhancement and segmentation techniques for detection of knee joint diseases: A survey. *Current Medical Imaging Reviews*, Vol. 14(5), 704–715. <https://doi.org/10.2174/1573405613666170912164546>
- Sadad, T., Munir, A., Saba, T., & Hussain, A. (2018). Fuzzy C-means and region growing based classification of tumor from mammograms using hybrid texture feature. *Journal of Computational Science*, 29, 34–45.
- Sáez, A., Acha, B., & Serrano, C. (2014). Pattern analysis in dermoscopic images. In *Computer vision techniques for the diagnosis of skin Cancer* (pp. 23–48). Springer.
- Safi, A., Baust, M., Pauly, O., Castaneda, V., Lasser, T., Mateus, D., . . . Ziai, M. (2011). Computer-aided diagnosis of pigmented skin dermoscopic images. Paper presented at the MICCAI International Workshop on Medical Content-Based Retrieval for Clinical Decision Support.
- Sangeetha, R., & Kalpana, B. (2011). Identifying efficient kernel function in multiclass support vector machines. *Training*, 2, 2.
- Sarker, M., Kamal, M., Rashwan, H. A., Banu, S. F., Saleh, A., Singh, V. K., . . . Radeva, P. (2018). SLSDeep: Skin Lesion Segmentation Based on Dilated Residual and Pyramid Pooling Networks. arXiv preprint arXiv: 1805.10241.
- Satheesha, T., Satyanarayana, D., Prasad, M. G., & Dhruve, K. D. (2017). Melanoma is skin deep: A 3D reconstruction technique for computerized dermoscopic skin lesion classification. *IEEE Journal of Translational Engineering in Health and Medicine*, 5, 1–17.
- Sharif, M., Khan, M. A., Faisal, M., Yasmin, M., & Fernandes, S. L. (2018). A framework for offline signature verification system: Best features selection approach. *Pattern Recognition Letters*.
- Sharif, M., Khan, M. A., Iqbal, Z., Azam, M. F., Lali, M. I. U., & Javed, M. Y. (2018). Detection and classification of citrus diseases in agriculture based on optimized weighted segmentation and feature selection. *Computers and Electronics in Agriculture*, 150, 220–234.
- Shlens, J. (2014). A tutorial on principal component analysis. arXiv preprint arXiv:1404.1100.
- Siegel, R. L., Miller, K. D., & Jemal, A. (2016). Cancer statistics, 2016. CA: A *Cancer Journal for Clinicians*, 66(1), 7–30.
- Waheed, S. R., Alkawaz, M. H., Rehman, A., Almazyad, A. S., & Saba, T. (2016). Multifocus watermarking approach based on discrete cosine transform. *Microscopy Research and Technique*, 79(5), 431–437. <https://doi.org/10.1002/jemt.22646>
- Wolner, Z. J., Yélamos, O., Liopyris, K., Rogers, T., Marchetti, M. A., & Marghoob, A. A. (2017). Enhancing skin Cancer diagnosis with dermoscopy. *Dermatologic Clinics*, 35(4), 417–437.
- Wu, J. T., Dernoncourt, F., Gehrmann, S., Tyler, P. D., Moseley, E. T., Carlson, E. T., . . . Celi, L. A. (2018). Behind the scenes: A medical natural language processing project. *International Journal of Medical Informatics*, 112, 68–73.
- Xu, H., Lu, C., Berendt, R., Jha, N., & Mandal, M. (2018). Automated analysis and classification of melanocytic tumor on skin whole slide images. *Computerized Medical Imaging and Graphics*, 66, 124–134.
- Yu, L., Chen, H., Dou, Q., Qin, J., & Heng, P.-A. (2017). Automated melanoma recognition in dermoscopy images via very deep residual networks. *IEEE Transactions on Medical Imaging*, 36(4), 994–1004.
- Yu, Z., Ni, D., Chen, S., Qin, J., Li, S., Wang, T., & Lei, B. (2017). Hybrid dermoscopy image classification framework based on deep convolutional neural network and fisher vector. Paper presented at the Biomedical Imaging (ISBI 2017), 2017 I.E. 14th International Symposium.
- Yuan, X., Situ, N., & Zouridakis, G. (2009). A narrow band graph partitioning method for skin lesion segmentation. *Pattern Recognition*, 42(6), 1017–1028.
- Zhang, Y., Qiu, M., Tsai, C.-W., Hassan, M. M., & Alamri, A. (2017). HealthCPS: Healthcare cyber-physical system assisted by cloud and big data. *IEEE Systems Journal*, 11(1), 88–95.
- Zhou, H., Schaefer, G., Sadka, A. H., & Celebi, M. E. (2009). Anisotropic mean shift based fuzzy c-means segmentation of deroscopy images. *IEEE Journal of Selected Topics in Signal Processing*, 6(1), 26–34.

How to cite this article: Khan MA, Akram T, Sharif M, et al. Construction of saliency map and hybrid set of features for efficient segmentation and classification of skin lesion. *Microsc Res Tech*. 2019;82:741–763. <https://doi.org/10.1002/jemt.23220>